Multi-therapeutic-activity selenium nanodot toward preventing brain injury and restoring neurobehavioral functions following hemorrhagic stroke

Yibin Zhang[1,2,3,4†], Xiaoyu Wang[5†], Xuegang Niu[1,2,3,4†], Haojie Wang[1,2,3,4], Yi Wu[1,2,3,4], Chunwang Li[1,2,3,4], Huimin Wang[1,2,3,4], Shen Lin[1,2,3,4], Dengliang Wang[1,2,3,4], Fuxin Lin[1,2,3,4], Peisen Yao[1,2,3,4], Yuanxiang Lin[1,2,3,4*], Dezhi Kang[1,2,3,4*] and Bin Gao[1,2,3,4*]

Abstract

Intracerebral hemorrhage is a lethal cerebrovascular disease, and the inevitable secondary brain injury (SBI) is responsible for serious disability and death. Perfect therapeutic goal is to minimize SBI and restore neurobehavioral functions. Recently, neuroprotection is highlighted to reduce SBI, but it still faces "Neuronal survival but impaired functions" dilemma. Herein, this work further proposes a novel combinational therapeutic strategy of neuroprotection and neurogenesis toward this goal. However, appropriate therapeutic agents are rarely reported, and their discovery and development are urgently needed. Selenium participates in various physiological/ pathological processes, which is hypothesized as a potential targeting molecule. To explore this effect, this work formulates an ultra-small selenium nanodot with a seleno-amino acid derived carbon dot domain and a hydrophilic PEG layer, surprisingly finding that it increases various selenoproteins levels at perihematomal region, to not only exert multiple neuroprotective roles at acute phase but promote neurogenesis and inhibit glial scar formation at recovery phase. At a safe dose, this combinational strategy effectively prevents SBI and recovers neurobehavioral functions to a normal level. Furthermore, its molecular mechanisms are revealed to broaden application scopes in other complex diseases.

†Yibin Zhang, Xiaoyu Wang and Xuegang Niu contributed equally to this work.

*Correspondence:
Yuanxiang Lin
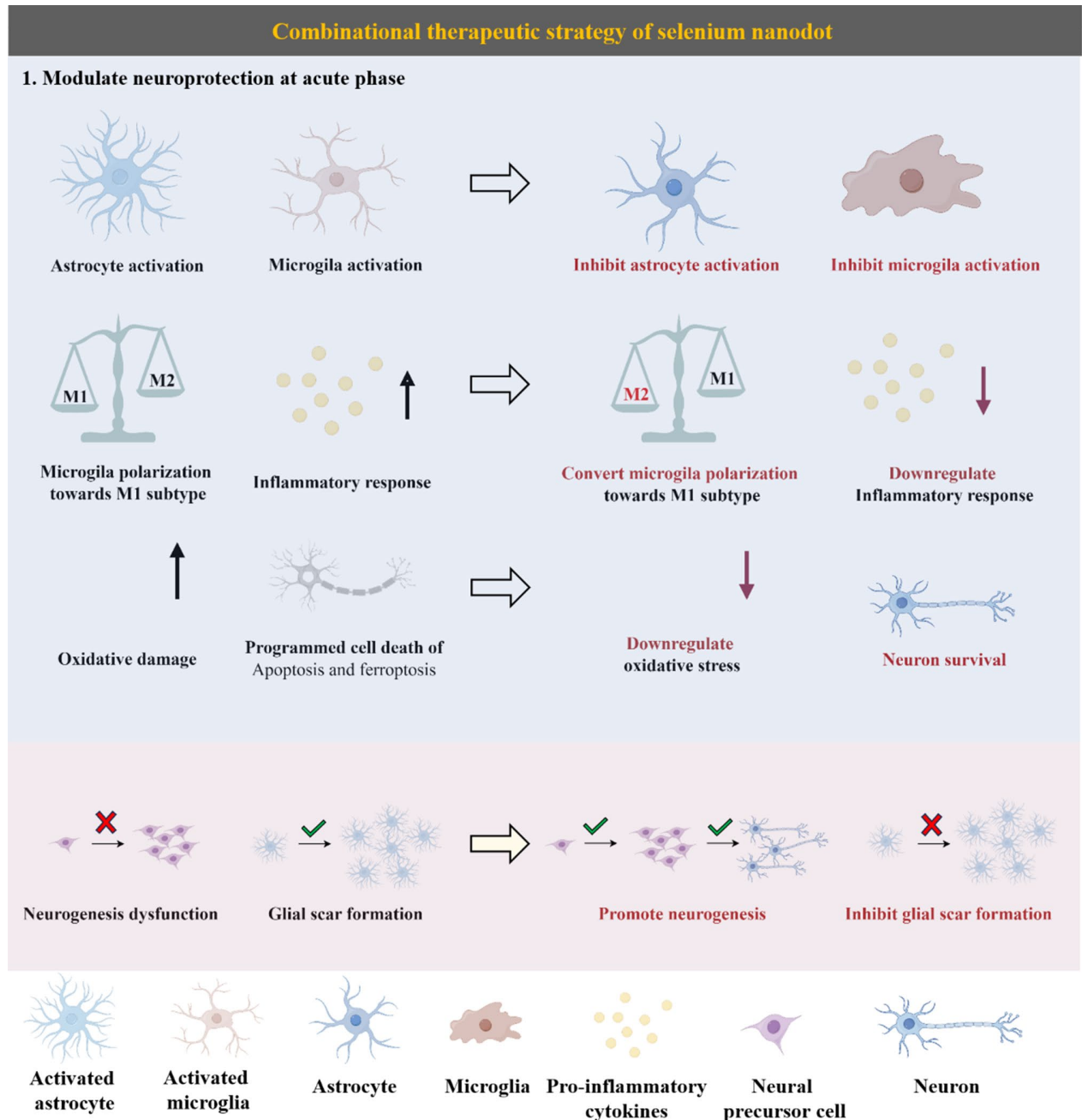lyx99070@163.com
Dezhi Kang
kdz99988@vip.sina.com
Bin Gao
GBIN000@163.com

Full list of author information is available at the end of the article

Graphical abstract

Combinational therapeutic strategy of selenium nanodot

1. Modulate neuroprotection at acute phase

Astrocyte activation — Microgila activation ⟹ Inhibit astrocyte activation — Inhibit microgila activation

Microgila polarization towards M1 subtype — Inflammatory response ⟹ Convert microgila polarization towards M1 subtype — Downregulate Inflammatory response

Oxidative damage — Programmed cell death of Apoptosis and ferroptosis ⟹ Downregulate oxidative stress — Neuron survival

Neurogenesis dysfunction — Glial scar formation ⟹ Promote neurogenesis — Inhibit glial scar formation

Activated astrocyte — Activated microglia — Astrocyte — Microglia — Pro-inflammatory cytokines — Neural precursor cell — Neuron

Introduction

Intracerebral hemorrhage (ICH), accounting for >28% of all stroke incidents, represents a lethal form of stroke with a high one-year mortality rate of 50% [1, 2]. Additionally, the survivors are commonly suffered from life-long poor neurofunctional outcomes, such as cognitive and behavioral dysfunctions, having brought heavy economic and health burdens to families and society [3, 4]. For inferior prognosis, the occurrence and development of secondary brain injury (abbreviated as SBI) are primarily responsible [5, 6]. Nevertheless, surgical treatment is not suitable for SBI, and also faces the serious

complications and risks, including infection, iatrogenic injury, secondary surgery [7]. Consequently, effective pharmacotherapy is imperative to achieve primary therapeutic goal of minimizing SBI and restoring neurobehavioral functions.

The past decades have witnessed an explosion of developing pharmacotherapies toward this therapeutic goal, mostly represented by either neuroprotection (i.e. certain anti-inflammatory/anti-oxidative drugs and their delivery nanosystems to alleviate inflammatory response and oxidative stress [8–12], small-molecule inhibitors/functional nanoenzymes to inhibit programmed cell death of neuron [13, 14]) or neurogenesis (i.e. gene/growth factor therapies to promote proliferation and differentiation of neural stem/precursor cells [15, 16]). Unfortunately, they have failed to acquire the convincing benefits in clinical trials [17, 18]. Furthermore, bioactive stem cells/exosomes are recently considered as hopeful therapeutic strategies benefiting from their potential to promote neural repair, but they are suffered from inadequate neuroprotective effect, low stability, low yield, and expensive price. Therefore, the new therapeutic strategy is urgently needed.

It is generally acknowledged that pathogenesis of SBI exhibits a cascading process over the first few days to weeks after ICH, and the essential pathological features primarily include resident immune system activation, uncontrolled inflammatory response and oxidative damage, programmed cell death of neuron represented as apoptosis/ferroptosis at acute phase [19], then adult neurogenesis dysfunction of neural stem/precursor cells as well as glial scar formation at recovery phase [11, 20]. These evidences definitely suggest that the pathogenesis of SBI is highly complex, involving multiple cellular/molecular/programmed cell death events. Even worse, these events dynamically change with pathological process, having exhibited spatiotemporal heterogeneity. However, the current drugs only modulate single one specific cellular/molecular/death target or pathological process, which are considered as the most important reason for the undesirable efficacy in reducing SBI and recovering neurobehavioral functions [21]. And thereby, it is hypothesize that the combinational therapy enabled by a multi-therapeutic-activity drug that is capable of both modulating neuroprotection and enhancing neurogenesis via intervening multiple pathologically relevant cells/molecules/programmed cell deaths from acute to recovery phases, is a potential strategy. Nevertheless, to date, there are still scant data regarding multi-therapeutic-activity drug design, combinational therapy evaluation and in-depth molecular mechanisms.

Selenium, an essential trace element widely found in living organisms, is recently found to serve selenoproteins as primary carriers, seleno-amino acids as redox catalytic sites to exert various physiological functions [22–26]. Although its modulatory effect on neuroprotection and neurogenesis via multiple pathways is unclear, we try to speculate it as a potential targeting molecule to develop new combinational therapeutic strategy. Unfortunately, natural selenoproteins have several disadvantages, which result in the loss of druggability. Firstly, blood-brain barrier (BBB) strictly restricts the biodistribution of selenoprotein as a biomacromolecule in the injuried brain [19, 27, 28]. Secondly, further endosomatic selenium transport into specific cell heavily relies on selenoprotein P-receptor interactions [26]. However, the limited receptor number causes the low selenium bioavailability inside injuried cells and insufficient pharmacological activity. Thirdly, natural selenoprotein exhibits poor formulation stability, making it difficult to maintain long-term bioactivity. Therefore, the new alternative to overcome selenium transport barrier and formulation stability is highly desirable to explore combinational therapeutic strategy.

As a proof of concept, we formulated an ultra-small selenium nanodot (denoted as SeNano) to explore combinational therapeutic effects. Endogenous selenomethionine provided selenium source and widely participated in selenium metabolism, herein the L-type or D-type selenomethionine was used as starting materials to prepare an ultra-small carbon dot framework by hydrothermal treatment, which could not only concentrate selenium to rationally simulate redox catalytic site for the support of exerting physiological functions, but be easier to overcome transport barrier due to ultra-small size advantage. Then, hydrophilic PEG segment was conjugated to the as-prepared carbon dot to improve formulation solubility and stability. Intranasal administration enabled SeNano to avoid BBB and quickly arrive in the injuried brain area following ICH. It was found that SeNano inhibited glia overactivation, converted M1-like pro-inflammatory to M2-like anti-inflammatory microglia, downregulated inflammatory factor and oxidative stress, finally blocked neuronal apoptosis and ferroptosis, exerting multiple neuroprotective roles and significantly increasing neuronal survivals at acute phase. More importantly, it also promoted the proliferation of neural precursor cells and neurogenesis, inhibited glial scar formation, and further improved neuronal repair and neurofunctional reconstruction during recovery. Consequently, this multi-therapeutic-activity selenium nanodot achieved therapeutic goal of preventing SBI and restoring neurobehavioral functions to a normal level following hemorrhagic stroke, where L-selenomethionine derived nanodot had a superior therapeutic effect than D-selenomethionine derived nanodot. In addition, it had satisfactory biosafety results. Our work not only offered a new combinational pharmacotherapy for hemorrhagic stroke management, but

further shed light on molecular mechanisms to broaden its application scopes in other complex diseases.

Materials and methods

Materials

Selenomethionine, D-Selenomethionine were supplied by Macklin Biochemical Technology Co., Ltd. Succinimidyl succinate-PEG-methoxy (NHS-PEG, 1000 Da) was purchased from JenKem Technology. Amiloride hydrochloride was purchased from Abcam. Chlorpromazine was provided by Sigma-Aldrich. Filipin III was purchased from Cayman Chemical. Dichlorodihydrofluorescein diacetate (DCFH-DA), TUNEL apoptosis assay kit and 4′, 6-diamidino-2-phenylindole dihydrochloride (DAPI) were obtained from Meilun Biotechnology Co., Ltd. Dulbecco's modified eagle medium (DMEM), fetal bovine serum (FBS), cell counting kit-8 (CCK-8), were ordered from Invitrogen Biotechnology Co., Ltd. The GSH assay kit and Iron assay kit were obtained from Solarbio Science & Technology Co., Ltd. Primary antibodies for immunofluorescence and immunohistochemistry experiments including GFAP (ab7260), Iba-1 (ab178847), CD206 (ab64693), CD86 (ab119857), TNF-α (ab183218), IL-6 (ab290735), IL-4 (ab225638), IL-10 (ab9969), 8-OHG (ab48508), NeuN (ab177487), 4-HNE (ab48506), MDA (ab27642), GPX4 (ab125066), BrdU (ab6326), DCX (ab18723), NOX2 (ab310337) were purchased as indicated. Other chemicals were analytical grade without further purification.

Preparation of SeNano

SeNano were prepared according to the synthetic method reported previously [29]. Firstly, L-selenomethionine (200 mg) was added into deionized water (10 mL), and then the pH of solution was adjusted to be ∼9 to facilitate the dissolution of L-selenomethionine. Afterwards, this was heated at 60 ℃ for 24 h to form brown solution, and then it was centrifuged at 8000 rpm for 15 min to collect supernatant, dialyzed (500 Da) for 24 h against deionized water and finally lyophilized to acquire L-selenomethionine derived carbon dot. Secondly, as-prepared L-selenomethionine derived carbon dot (100 mg) was dissolved in PBS (10 mL, pH=7.4), and then NHS-PEG (30 mg) was added to stir for 6 h at room temperature. Then, this solution was dialyzed (1000 Da) for 24 h against deionized water and lyophilized to acquire L-SeNano agent. Similarly, D-SeNano agent was prepared according to this above process using the D-selenomethionine as selenium source.

Physicochemical characterizations of SeNano

X-Ray Photoelectron Spectroscopy (XPS) was performed to study chemical composition and structure. Inductively Coupled Plasma -Mass Spectrometry (ICP-MS) was conducted to confirm selenium content. High-Resolution Transmission Electron Microscopy (HRTEM) was used to observe the morphology, size and lattice structure. Fluorescence spectrophotometer was tested to investigate luminescent property. Zetasizer Nano ZS was performed to examine the Z-average diameter and zeta potential. Electron Paramagnetic Resonance (EPR) was performed to study the redox-regulating property (1. Hydroxyl radicals were generated by Fenton reaction with 1 mM H_2O_2 and 1 mM $FeSO_4$ system. Samples were added into the obtained hydroxyl radicals solution. Then, the DMPO scavenger was added into the mixed solution to support test on the apparatus; 2. Singlet oxygen was generated by 1 mM peroxymonosulfate (PMS) system. Samples were added into the obtained singlet oxygen solution. Then, the TEMP scavenger was added into the mixed solution to support test on the apparatus; 3. Superoxide anions were generated by 1 mM H_2O_2 and light irradiation system. Samples were added into the obtained superoxide anions solution. Then, the DMPO scavenger was added into the mixed solution to support test on the apparatus.)

Cell culture and cell model of ICH

SH-SY5Y, Bend.3, BV2 and HT22 cell lines were obtained from the Cell Bank of Typical Culture Collection of Chinese Academy of Sciences for the cell culture in a 5% CO_2 incubator at 37 ℃. To establish the cell model of ICH, hemin was used to stimulate cells. In detail, cells were seeded in 96-well plate and cultured for 24 h with complete DMEM, and then different concentrations of hemin solutions were added for 6 h of culture. Afterwards, culture medium was replaced with fresh medium containing CCK-8 agent, and continued to incubate for 2 h. Finally, the absorbance value was measured at 450 nm via a microplate reader to reflect cell viability for cell survival evaluation.

Cellular uptake pathway of SeNano

Flow cytometry was used to study the cellular uptake pathway of SeNano in SH-SY5Y cells. SH-SY5Y cells were plated in 6-well plate (2.5×10^5 cells/well) and cultured for 24 h. Then, different endocytosis inhibitors, chlorpromazine (30 µM), amiloride hydrochloride (30 µM) or filipin III (5 µg/mL), were added for 1 h of treatment. Next, the cells were washed three times with PBS, and Cy5.5-labeled SeNano were added for 4 h of treatment. Finally, cells were washed three times with PBS and resuspended in PBS following the trypsinization and centrifugation, for flow cytometry analysis.

In vitro evaluation of ROS regulation

DCFH-DA assay kit was used to examine intracellular ROS level for in vitro evaluation of ROS regulation. HT22 cells were treated with hemin (60 µM) to establish

cell model of ICH. Next, these cells were incubated with different concentrations of SeNano for 24 h, and then DCFH-DA was added for 30 min. Subsequently, cells were washed with PBS three times. The resulting cells were trypsinized and collected in PBS for fluorescence microscope observation (green channel) and analysis of mean fluorescence intensity by Image J.

In vitro evaluation of neuroprotective role
HT22 cells were pre-treated with hemin (60 μM) to establish cell model of ICH. The cells were incubated with different concentrations of SeNano for 24 h, and then culture medium was replaced with fresh medium containing CCK-8 agent and continued to incubate for 2 h. Finally, the absorbance value was measured at 450 nm *via* a microplate reader to reflect cell viability for in vitro evaluation of neuroprotective role.

Animal model of ICH and therapy strategy
To better mimic clinical ICH, we applied autologous blood method to establish ICH model in mice as previously reported work [30]. Herein, C57BL/6 mice at age of 10–12 weeks were used and they were purchased from Silake Experimental Animal Limitied Liability Company (Shanghai, China). Mice were randomly divided into five groups (sham, saline, L-SeNano, D-SeNano, Edaravone/Dexborneol), where ICH model was performed for the later four groups. Before ICH surgery, mice were supplied with natural circadian rhythm and access to sufficient food and water. Animal experiment was conducted according to Animal Protection Guidelines of Fujian Medical University (IACUC FJMU 2024-Y-0857), which was also conformed to the "Guide for the Protection and Use of Experimental Animals" of American National Institutes of Health.

In detail, mice were firstly fully anesthetized with gas anesthesia and then maintained the state of anesthetization by injecting 1.5% isoflurane. The mice were immobilized at a brain stereotaxic instrument, and a burr hole was drilled on the right side of the skull, located 2.3 mm lateral to the midline and 0.5 mm anterior to bregma. Then, the pre-obtained autologous blood (30 μL) from angular vein was slowly injected for 5 min at a depth of 3 mm and at a rate of 1 μL/min. Subsequently, the needle was advanced to 3.7 mm depth for another 5 min of in situ retention to prevent blood efflux. The remaining blood (25 μL) was again injected at a rate of 1 μL/min. Finally, the suture was sealed by bone wax. As contrast, the mice of sham group were injected with saline to the basal ganglia. During ICH surgery, environmental temperature was maintained at ∼25 ℃, and after surgery mice were placed at a temperature-controllable blanket and then housed a standard condition, including 12 h of light-dark cycle, access to food and water. For therapy, the mice of each group (saline, L-SeNano, D-SeNano, Edaravone/Dexborneol) were intranasally administrated with different drugs at 4 mg/kg dose once every three days. The mice in sham group were performed with the same procedure but without drug administration.

In vivo and ex vivo evaluations of biodistribution
Cy7-labeled SeNano (4 mg/kg) were intranasally administered into the mice suffered from ICH. After the differemt time points (30 min, 1 h, 12 h, 24 h), the mice were visualized for in vivo fluorescence imgaing. Then, mice were sacrificed to collect brains and major organs (heart, liver, spleen, lung, kidney) for ex vivo fluorescence imgaing. These imgaging results were used to monitor the biodistribution of SeNano.

In vivo evaluations of intervention effects at acute and recovery phases
To evaluate intervention activities, immunofluorescence staining, immunohistochemistry staining and ELISA assays were performed. For immunofluorescence staining, the mice were transcardially perfused with saline and 4% paraformaldehyde (PFA), and brain sections were collected and fixed by 4% PFA. After the sections of brain tissue with ∼25 μm thickness were prepared, the Triton X-100 permeation and serum treatment were performed for further primary antibodies incubation at 4 ℃ overnight, incluidng anti-GFAP antibody, anti-Iba-1 antibody, anti-CD206 antibody, anti-CD86 antibody, anti-8-OHG antibody, anti-NeuN antibody, anti-4-HNE antibody, anti-MDA antibody, anti-GPX4 antibody, anti-BrdU antibody (Prior to staining, BrdU was continuously administered through intraperitoneal injection at 50 mg/kg for 14 days), anti-DCX antibody, anti-NOX2 antibody. Next, the sections were washed with PBS three times, and then incubated with Alexa Fluor-conjugated secondary antibody. And DAPI was used as a nuclear stain. For immunohistochemistry staining, the sections of brain were stained with TNF-α, IL-6, IL-4 and IL-10. For ELISA assay, the brain tissues at perihematomal region were collected to support GSH assay kit and Iron assay kit tests according to their instruments for examining GSH and iron contents. For the TEM observations of ferroptosis, mice were perfused with pre-cooled PBS and their brains were promptly removed and fixed in 2.5% glutaraldehyde. The ipsilateral parietal cortex was removed, and then fixed in 2.5% glutaraldehyde overnight at 4 ℃. It was subsequently postfixed in 1% OsO_4 for 2 h, washed three times in cacodylate buffer, stained in 1% uranylacetate for 1 h, then dehydrated in the grading concentrations of ethanol, and finally embedded in Epon. Thin tissue sections were sliced using an ultramicrotome from Leica, then mounted on EM grids, stained with uranium acetate and lead citrate, and finally observed under TEM.

In vivo evaluation of combinational therapeutic strategy

Nissl staining was performed to detect nissl bodies in the cytoplasm of neurons, which was an indicator of neuronal integrity and number. Mice were sacrificed under anesthetized, and their brains were perfused in situ with 10% formalin. Then, brains were soaked in 4% paraformaldehyde solution at 4 °C for 72 h. Brain tissues adjacent to hematoma were embedded in 30% paraffin, and cut into 20 μm thick sections. These sections were deparaffinized with xylene and graded alcohol. Toluidine blue was used according to a standard protocol. Sections were observed and photographed under an optical microscope.

Modified neurologic severity score (mNSS) was used to assess motor dysfunction using a blinded scoring method. The mNSS was a composite score in a range of 0 to 18, including the impaired motor function, sensory acuity, reflex, and balance function. A lower score represented better neurological recovery. Each animal was tested at the same time daily by the same experimenter blinded to experimental condition.

Locomotor behaviors were assessed using open field test. Mice were placed in an opaque, square (length 50.0 cm, width 50.0 cm), white acrylic arena with 40 cm of high wall, and allowed to freely explore for 10 min. The center of arena was defined as a square 20.0×20.0 cm in the middle of the arena. Mice were placed in the corner of open-field arena. The overhead camera recorded horizontal movements over a 10 min of period by the ANY-maze software. After conducting each experiment, make sure thoroughly clean the box with 75% of ethanol in order to eliminate any mouse excrement and odor present. Once ethanol was evaporated, the following experiments will be conducted. To evaluate locomotor activity, we measured total distance traveled in the arena and the average velocity in m/s by ANY-maze software.

Spatial working memory was assessed using spontaneous alternation Y maze. The Y maze was made of the white opaque acrylic with three symmetrical arms (arm length 30.0 cm, width 5.0 cm, height 15.0 cm) at an angle of 120°. The mice with no previous exposure or habituation to maze, were placed at the center of the maze and allowed to explore freely apparatus for 5 min. Mice, naturally prone to explore novel environment, had a strong tendency to choose an unexplored arm over the recently explored one and therefore alternated arm choices on successive trials. Alternations or triads were defined as a successive entry into three consecutive arms (e.g. ABC and CAB), and percent alternation was calculated as the ratio of the number of triads to the possible alternations (i.e. total number of entries minus two) multiplied by 100. Mice were video-tracked and their centerpoint had to pass the entry zone to count for a triad. Apparatus was randomly rotated between tests to avoid arm preference.

Spontaneous alternation rates were assessed by ANY-maze software.

Study of molecular mechanism

Brain tissue samples at perihematomal region (Day 3) and at subventricular zone (Day 28) were sent to Novogene Co., Ltd. (Beijing, China) for RNA-seq library preparation. After clustering, we performed transcriptome sequencing on DNBSEQ-T7 platform that generated raw reads. Data quality was assessed by the FastQC tool after removal of adaptor sequences, ambiguous "N" nucleotides (proportion of "N" > 5%), and low-quality sequences (quality score < 10). The ggplotR package was used to identify StringTie genes. Differences were statistically significant threshold for |log2 fold change| ≥ 1 or $P < 0.05$. GO enrichment, KEGG pathway, heatmap and volcanic figure were carried out at https://www.bioinformatics. com.cn (China).

Biosafety assessment

Biosafety was evaluated at cell, blood and organ levels, respectively. Firstly, CCK-8 assay of common cell type in brain was performed to evaluate the cytotoxicity of SeNano, including mouse brain microvascular endothelial cells (Bend.3), mouse microglial cells (BV2) and mouse hippocampal neuronal cells (HT22). Cells were seeded in 96-well plate and cultured for 24 h with complete DMEM. Then, cells were treated with different concentrations of SeNano for 24 h. In contrast, these cells treated with PBS were used as negative control. Afterwards, culture medium was replaced with fresh medium containing CCK-8 agent and continued to incubate for 2 h. Finally, the absorbance value was measured at 450 nm *via* a microplate reader to reflect cell viability for biosafety evaluation at the cell level. Secondly, blood was extracted from inner canthus at day 28 for blood routine and blood biochemical tests to study the physiological index and liver and kidney functions, which could evaluate biosafety at the blood level. Finally, the primary organs, including heart, liver, spleen, lung and kidney, were collected for H&E staining at day 28 to study the organ injury situation, which was used to evaluate biosafety at the organ level.

Ethical issues on animal experiments

The animal experiments were conducted according to Animal Protection Guidelines of Fujian Medical University (IACUC FJMU 2024-Y-0857), which were also conformed to the "Guide for the Protection and Use of Experimental Animals" of American National Institutes of Health.

Zhang *et al. Journal of Nanobiotechnology*   (2024) 22:564

Page 7 of 23

Statistical analysis

Statistical results were analyzed through Unpaired Student's t test (two-tailed) for comparison between unpaired two-groups, and one-way analysis of variance (ANOVA) test for multigroup data comparison. The form of mean±SEM was used to show data, with statistical significance at $*P<0.05$, $**P<0.01$, $***P<0.001$, $****P<0.0001$.

Results and discussion

Formulation and characterizations of SeNano

Given that the endogenous selenomethionine could provide selenium source and widely participated in selenium metabolism, this work selected selenomethionine as starting materials to formulate SeNano agent. Herein, as shown in Fig. 1A, a facile preparation method of ultrasmall carbon dot was developed through the hydrothermal treatment of selenomethionine under mild condition. On one hand, this method concentrated seleno-amino acid to enrichment domain to rationally simulate the redox catalytic site of selenoprotein. On the other hand, this could also generate ultra-small sized particle, which

was beneficial to overcome transport barrier and increase bioavailability [31]. Afterwards, to increase formulation solubility and stability, PEG segment was conjugated to as-prepared carbon dot, which was used to simulate hydrophilic domain and assist to increase pharmacotherapy performance. In this work, the PEG conjugated carbon dot was denoted as SeNano to inhert physiological functions and solubility of nature selenoprotein, and further to enhance its formulation stability and transport capability, where the L-type or D-type selenomethionine generated L-SeNano or D-SeNano to explore the influence of starting material chirality on therapeutic effect.

To verify the formulation of SeNano, the chemical composition was studied using X-Ray Photoelectron Spectroscopy (XPS). SeNano were mainly composed of carbon, nitrogen, oxygen and selenium elements according to the typical peaks of C1s, N1s, O1s and Se3d (Fig. 1B). Further, the C1s was fitted into four peaks: C-Se (~283.3 eV), C-C (~284.8 eV), C-O/C-N (~286.4 eV) and O=C$-$N (~287.7 eV) from Fig. 1C-D, and the N1s was fitted into two peaks: pyridine N and NH_2 (~398.0 eV) and O=C$-$N (~400.1 eV) from Fig. 1E-F.
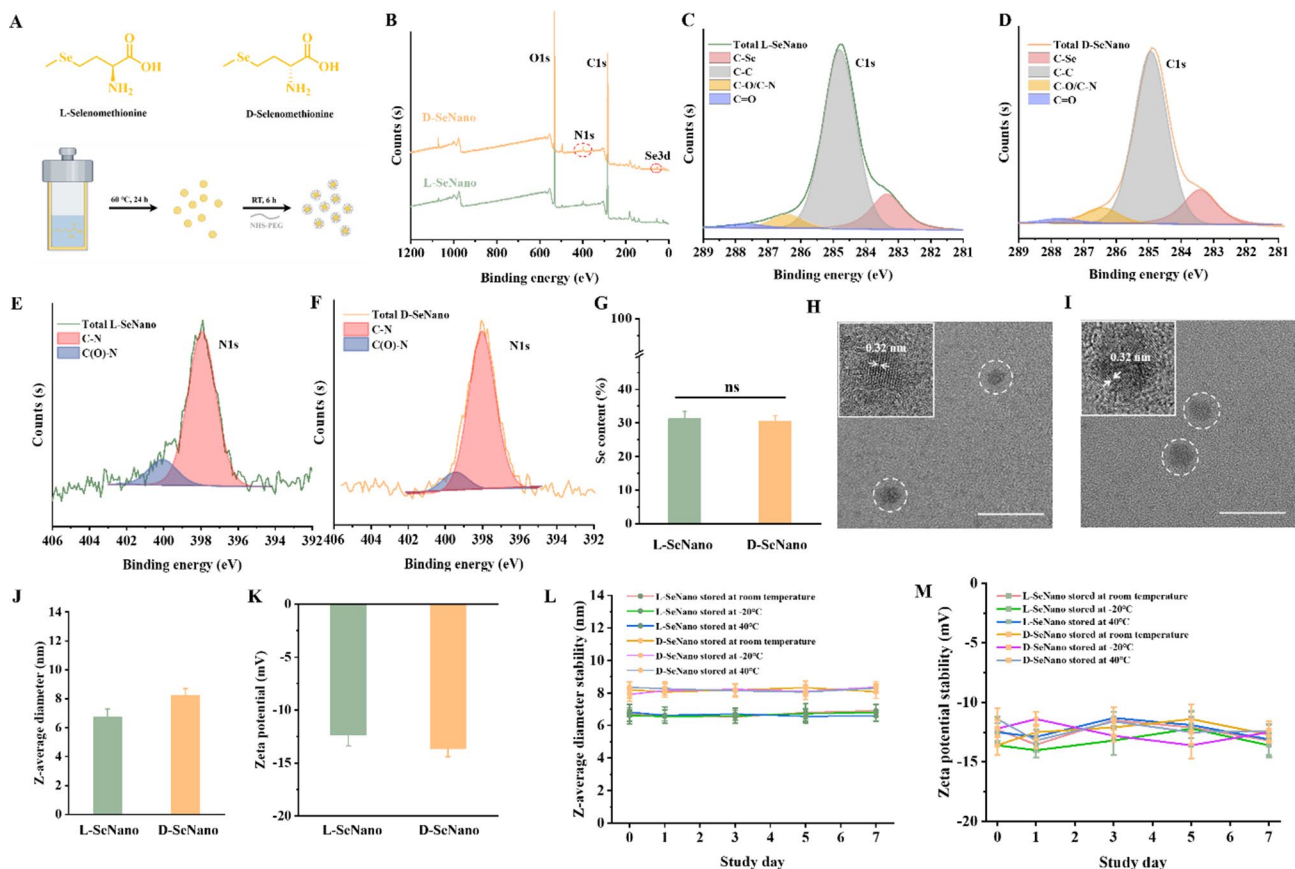

Fig. 1 Physicochemical characterizations of SeNano. (**A**) Schematic illustration of SeNano preparation. (**B**) XPS spectra of SeNano, and (**C-F**) high-resolution spectra of C1s, N1s. (**G**) Se content of SeNano detected by ICP-MS. (**H, I**) Microscopic morphology of SeNano observed by High-Resolution TEM. Scale bar: 10 nm. (J, K) Z-average diameter and zeta potential of SeNano in PBS (10 mM, pH=7.4) tested by Zetasizer Nano ZS. (**L, M**) Formulation stability of SeNano at different storage time and temperature

These indicated that hydrothermal treatment induced carbonization and amidation reactions to prepare carbon dot due to the appearance of pyridine N and $O=C-N$ peaks, and also illustrated that PEG segment was conjugated to the surface of carbon dot to successfully prepare SeNano resulting from the appearance of C-O peak. Fortunately, the two-step preparation didn't have an obvious influence on the original selenium structure of C-Se, and SeNano had $\sim 31\%$ selenium content detected by Inductively Coupled Plasma -Mass Spectrometry (ICP-MS) (Fig. 1G), which were in favour of exerting physiological functions. In addition, we examined SeNano morphology using High-Resolution Transmission Electron Microscopy (TEM), observing that SeNano had the spherical morphology and ultra-small size (uniform diameter of <10 nm) in Fig. 1H-I. After amplification, lattice structure with a typical lattice spacing of 0.32 nm was found, which was in accordance with spacing between graphene layers (002 facet) [32], also reflecting that carbonization reaction was successfully performed to support the formation of selenium-concentrated domain. Besides, it was tested that SeNano had excitation wavelength -dependent fluorescence property, and this also confirmed successful carbonization process (Fig. S1 and S2). Above results could show that starting material chirality didn't affect preparation process of SeNano becasue L-SeNano and D-SeNano had similar chemical composition and structure. Next, the surface-charged property and particle size were tested by Zetasizer Nano ZS after SeNano were dissloved in PBS (10 mM, pH=7.4), showing that L-SeNano had ~ 6.7 nm of Z-average diameter and $\sim$ -12.3 mV of zeta potential, while D-SeNano had ~ 8.2 nm of Z-average diameter and $\sim$ -13.6 mV of zeta potential (Fig. 1J-K). The ultra-small size and weak negative zeta potential were applicable for the endosomatic selenium transport into the injured brain and cell. Then, we investigated influence of storage time and temperature on formulation stability. As shown in Fig. 1L-M, Z-average diameter and zeta potential of SeNano didn't change obviously within 7 days, and the storage temperature at -20 ℃, RT, 40 ℃ also had no significant influence. Furthermore, when SeNano were incubated in medium containing 10% FBS, their Z-average diameter still maintained stable within 72 h (Fig. S3). These results implied that SeNano exhibited good formulation stability.

Functionality evaluations of SeNano

We then performed functionality evaluations of SeNano. Firstly, redox-regulating property was evaluated by Electron Paramagnetic Resonance (EPR), showing that SeNano effectively scavenged multiple reactive oxygen species (ROS) components, and its scavenging efficiency was $\sim 40\%$ for singlet oxygen, $\sim 74\%$ for hydroxyl radical, $\sim 45\%$ for superoxide anion, where L-SeNano

and D-SeNano almost showed the same performance (Fig. 2A-D). Beyond redox-regulating property, we wondered whether SeNano could increase selenoproteins levels in vivo. We established ICH model of mice and performed intranasal administration of SeNano, enabling various selenoproteins levels to increase at perihematomal region by the bulk RNA sequencing, where L-SeNano exhibited the largely stronger capability than D-SeNano (Fig. 2E). To further confirm this result, immunofluorescence staining of typical selenoprotein GPX4 was performed, observing that L-SeNano had great ability to increase GPX4 level, which was ~ 7.3 times of saline, and ~ 2.7 times of D-SeNano (Fig. 2F-G). This reflected that L-SeNano could not only exert redox-regulating property, but increase selenoproteins levels probably because it derived from the L-type natural selenomethionine and offered selenium source to promote selenoprotein biosynthesis. However, D-type selenomethionine of D-SeNano couldn't be used as selenium source.

Endosomatic selenium uptake into cells relied on selenoprotein P-receptor interactions [26], and the limited receptor number caused low selenium bioavailability inside injured cells and insufficient pharmacological activity. It was hoped that SeNano could overcome this limitation. Next, we investigated the cellular uptake property of SeNano in SH-SY5Y cell and results were shown in Fig. 2H-J. By quantitative analysis of flow cytometry, we found that L- SeNano and D-SeNano entered almost 100% of cells, but their uptake capability reflected by mean fluorescence intensity (MFI) was different, showing the stronger uptake of L-SeNano. Theoretically, PEG modification enabled nanomedicine to enter cells by endocytosis pathway. Therefore, we further explored influence of endocytosis inhibitors on cellular uptake, where chlorpromazine, amiloride hydrochloride, flipin III were used to inhibit the endocytosis pathway associated with clathrin, macropinocytosis, and caveolae, respectively. It was evidenced that L-SeNano and D-SeNano were primarily via caveolae-mediated endocytosis, which were beneficial to overcome the limitation of endosomatic selenium uptake.

Finally, we established cell model of ICH to preliminarily study the effect of SeNano on intracellular ROS level and cell survival. Hemin pre-treatment was used to establish cell model, and we studied the relationship of the hemin concentration gradient and cell survival, showing that the survival rate gradually decreased from $\sim 100\%$ to $\sim 27\%$ with hemin concentration increasing from 0 to 100 μM, in which hemin (60 μM) pre-treatment was screened to generate cell model with $\sim 55\%$ survival rate (Fig. S4). A large amount of intracellular ROS was generated in the cell model, and then the ROS level was decreased by SeNano treatment (Fig. 2K-L). L-SeNano exhibited a markedly stronger ROS-eliminating effect
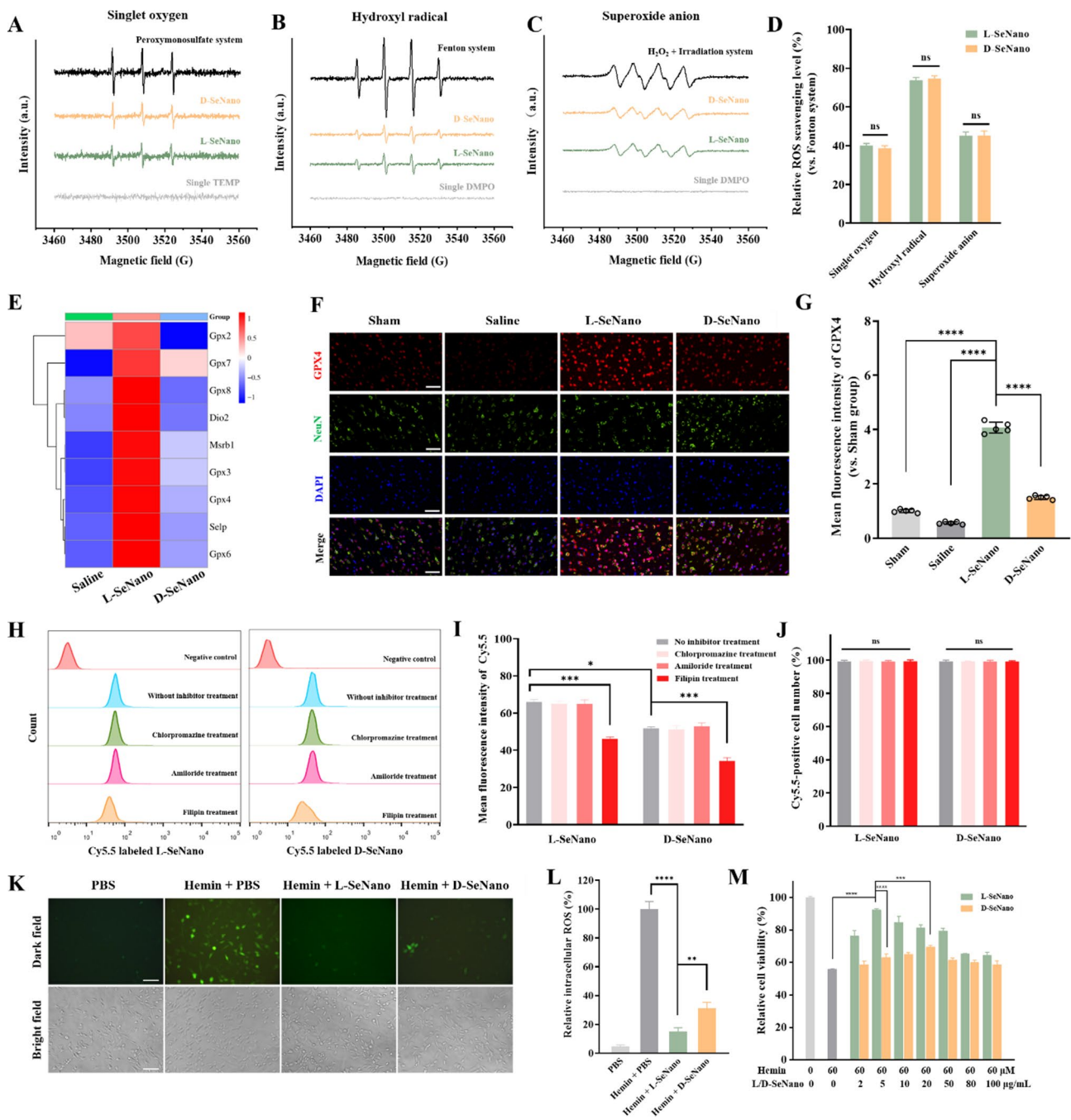
Fig. 2 Functionality evaluations of SeNano. (**A-C**) Redox-regulating property of SeNano analyzed by EPR, including (**A**) singlet oxygen, (**B**) hydroxyl radical, (**C**) superoxide anion. (**D**) Quantitative integral result of EPR spectra reflecting the ROS scavenging level of SeNano. (**E**) Various selenoproteins levels at perihematomal region tested by RNA sequencing at day 3. (**F**, **G**) Representative immunofluorescence staining of GPX4 (red)/NeuN (green)/DAPI (blue) and quantitative analysis of mean fluorescence intensity of GPX4 at perihematomal region at day 3. Scale bars: 50 μm. (**H-J**) Flow cytometric analysis of cellular uptake of SeNano by SH-SY5Y cell pre-treated with various endocytosis inhibitors, and quantitative analysis of mean fluorescence intensity and positive cell number. (**K**, **L**) Intracellular ROS visualized by DCFH-DA probe upon various treatments, and quantitative analysis of mean fluorescence intensity reflecting intracellular ROS level. Scale bars: 200 μm. (**M**) Neuronal survival upon various treatments examined by CCK-8 assay. The data were exhibited as mean ± SEM, and analyzed by a one-way ANOVA with Tukey's multiple comparisons

than D-SeNano, benefiting from its improved ability to increase anti-oxidative selenoprotein levels and cellular uptake. Further, SeNano could also save cell survival. L-SeNano achieved the highest survival rate of ∼92.3%

at 5 μM low concentration, while D- SeNano achieved the highest ∼79.5% even at 20 μM high concentration (Fig. 2M). Therefore, the L-SeNano exhibited potent effect on inhibiting neuronal death.

Above all, our designed SeNano, particularly L-SeNano, exhibited some key advantageous properties, i.e. (1) good formulation stability with less susceptibility on storage time and temperature, (2) ultra-small size and weak negative zeta potential with support of endosomatic selenium transport into injured brain, (3) combined redox-regulating property assigned to anti-oxidative nature of selenium element and intracellualr selenium source for selenoprotein biosynthesis, (4) enter cells via the caveolae-mediated endocytosis without selenium uptake limitation based on selenoprotein P-receptor interactions. (5) significantly inhibiting cell death. These were highly conducive to increase druggability of SeNano, which was hoped to exert its therapeutic effect and safety in subsequent animal experiments.

Intranasal administration of SeNano to brain following ICH

The BBB was an essential obstacle for the drug development of central nervous system diseases owing to the existence of tight junctions between brain microvascular endothelial cells. Though the ICH could destroy BBB to improve drug permeability, this only had a narrow time window. And long-term drug administration still needed to overcome the BBB obstacle [19, 27, 28].

Recently, the emerging intranasal administration was found to be BBB-independent and could directly deliver drugs into brain via olfactory and trigeminal pathways, which was considered as a promising intracerebral drug delivery technology [33–35]. Moreover, benefiting from the decreased systemic circulation, this strategy was in favour of the optimized therapeutic effect at a low dose, and exhibited high clinical translation value. Therefore, intranasal administration of SeNano was used for combinational therapy after ICH. Cy7-labeled SeNano were intranasally administered into mice for the analysis of IVIS fluorescence imaging system, where the distinct fluorescence signal was observed in brain within 1 h (Fig. 3A-B). Besides, we collected brain tissues at 1 h after intranasal administration, finding that selenium content significantly increased (Fig. S5). These could confirm quick transport of SeNano into brain and supported short onset time. And there were no obvious fluorescence differences and selenium contents between L-SeNano and D-SeNano, indicating their similar biodistribution in brain. Further, primary organs were isolated for ex vivo fluorescence imaging, observing that SeNano also distributed in liver and kidney (Fig. 3C) probably because a portion of SeNano were actually uptaken by
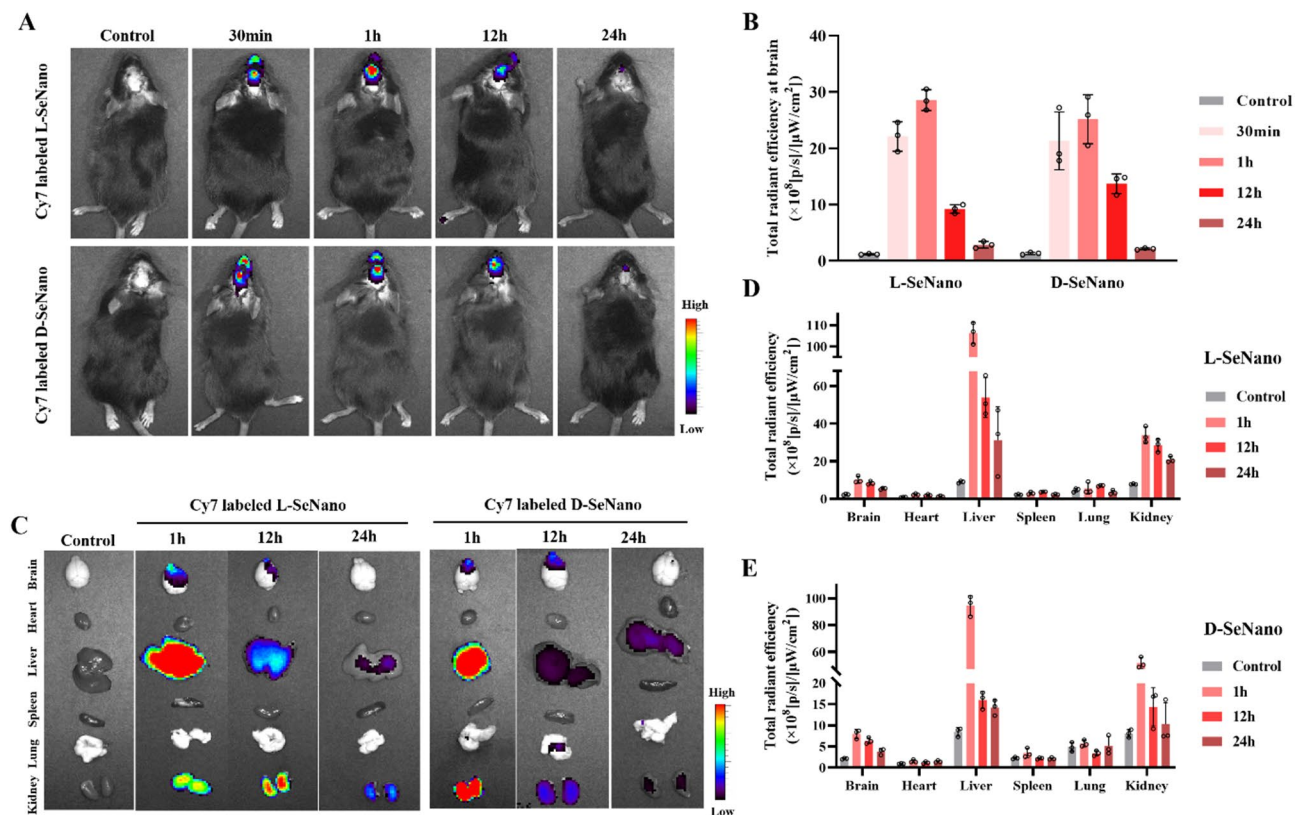

Fig. 3 Intranasal administration of SeNano to the brain. (**A**, **B**) In vivo fluorescence images of mice intranasally administrated with Cy7-labeled SeNano at different time points, and the quantitative analysis of total radiant efficiency in brain. (**C-E**) Ex vivo fluorescence images of isolated brains and major organs at different time points, and quantitative analysis of total radiant efficiency. The data were exhibited as mean ± SEM

the capillary networks at nasal mucosa and entered into systemic circulation. Fortunately, fluorescence signals in liver and kidney were largely reduced after 24 h (Fig. 3D-E), indicating that the SeNano were either cleared by liver or metabolized by urinary system.

Intervention effect of SeNano on neuroprotection at acute phase

At acute phase, the resident immune systems, mainly including microglia and astrocyte, initially responded to pathological changes, and were overactivated to release excessive cytotoxic inflammatory factors and ROS, which triggered uncontrolled inflammatory response and oxidative damage, and eventually contributing to programmed cell death of neuron. Immunofluorescence staining results revealed the significant infiltration and activation of microglia and astrocyte at day 3 following ICH, as Iba-1 and GFAP positive cells were

upregulated (Fig. 4A-D). The activated microglia exhibited an enlarged cell body, while the reactive astrocyte showed an increase of processes and a hypertrophic change in cell body. This also induced a shift of microglia towards M1-type polarization assigned to the downregulation of CD206/CD86 ratio (Fig. 4E-F), which could create a pro-inflammatory microenvironment to increase pro-inflammatory cytokines TNF-α and IL-6 levels, and decrease anti-inflammatory cytokines IL-4 and IL-10 levels (Fig. 5A-E). Moreover, this also exacerbated oxidative damage to neuronal DNA/RNA because the upregulated 8-OHG was mainly localized in neuron (Fig. 5F-G). Upon various treatments, L-SeNano was found to simultaneously intervene the above multiple pathogenesis, reflected by effectively reducing the glial cells activation, converting microglia polarization towards the M2 anti-inflammatory type, decreasing pro-inflammatory cytokines while increasing anti-inflammatory cytokines
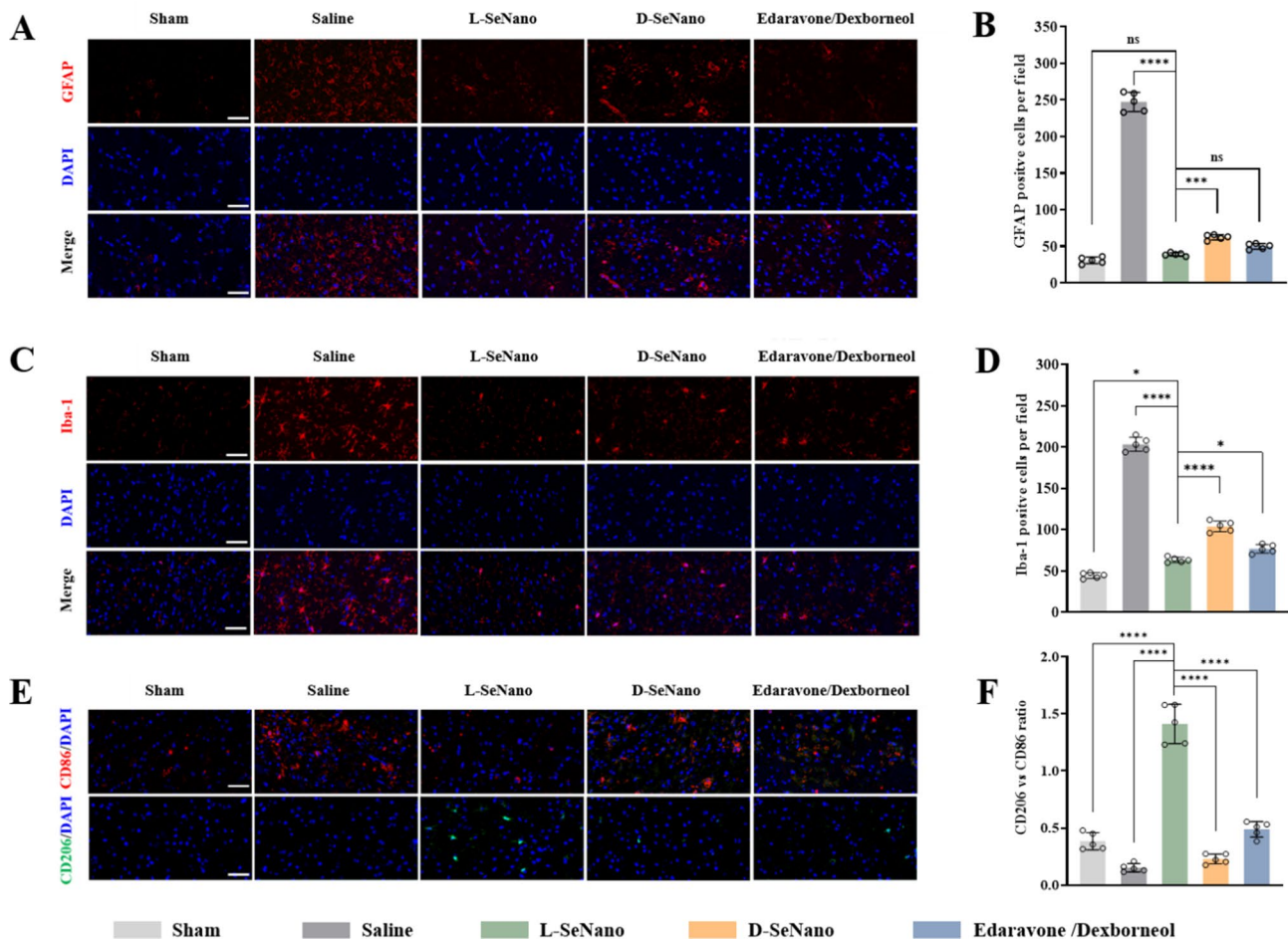

Fig. 4 Intervention effect of SeNano on glial cells activation and microglia polarization following ICH. (**A**, **B**) Representative immunofluorescence staining of GFAP (red)/DAPI (blue) reflecting astrocyte activation, and quantitative analysis of GFAP positive cells at perihematomal region at day 3. Scale bars: 50 μm. (**C**, **D**) Representative immunofluorescence staining of Iba-1 (red)/DAPI (blue) reflecting microglia activation, and quantitative analysis of Iba-1 positive cells at perihematomal region at day 3. Scale bars: 50 μm. (**E**, **F**) Representative immunofluorescence staining of CD86 (red)/DAPI (blue) and CD206 (green)/DAPI (blue) reflecting microglia polarization, and quantitative analysis of CD206/CD86 ratio at perihematomal region at day 3. Scale bars: 50 μm. The data were exhibited as mean ± SEM, and analyzed by a one-way ANOVA with Tukey's multiple comparisons
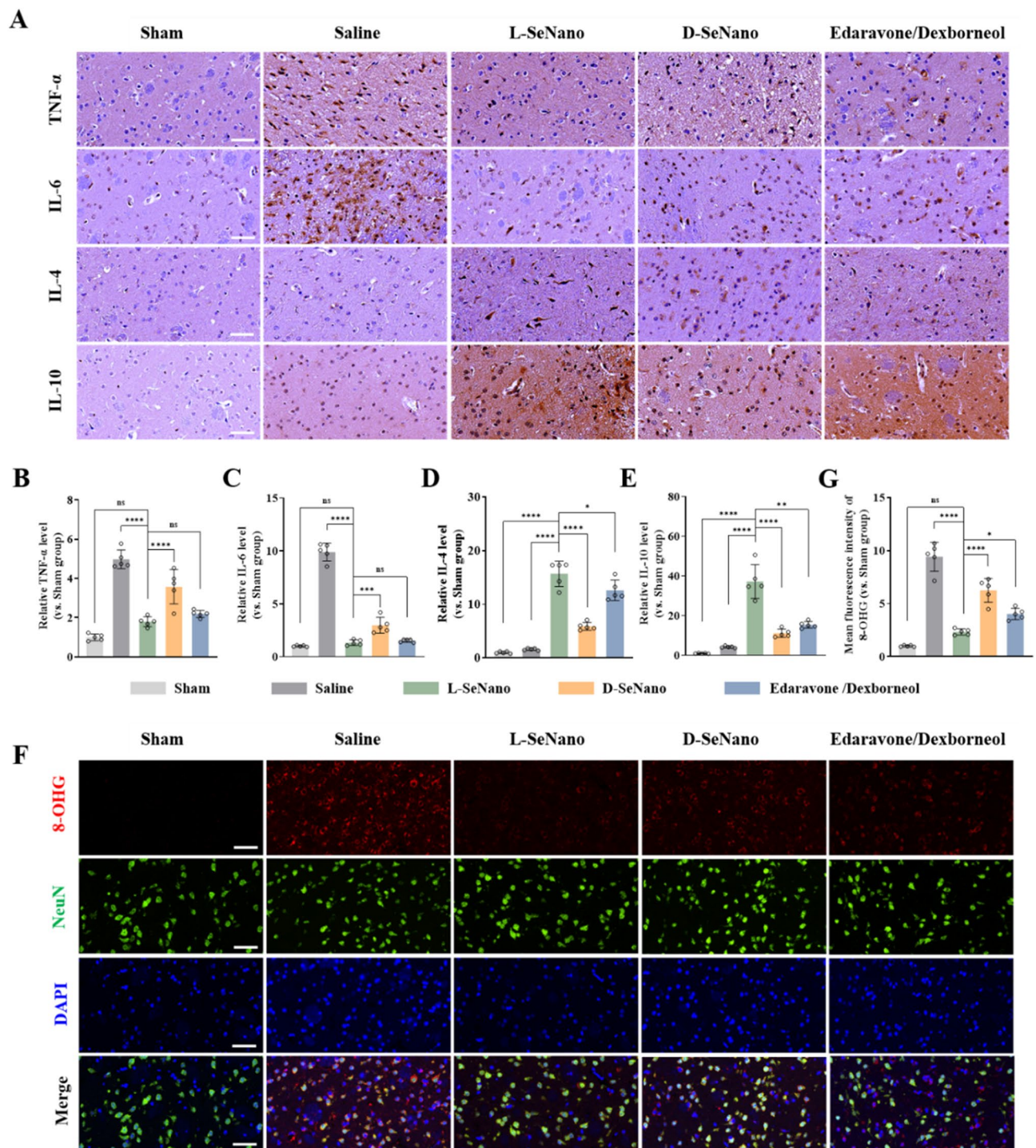
Fig. 5 Intervention effect of SeNano on inflammatory response and oxidative damage following ICH. (**A**) Representative immunohistochemical staining of pro-inflammatory cytokines (TNF-α, IL-6) and anti-inflammatory cytokines (IL-4, IL-10) at perihematomal region at day 3, indicating the inflammatory response. Scale bars: 50 μm. (**B**) Quantitative analysis of TNF-α level. (**C**) Quantitative analysis of IL-6 level. (**D**) Quantitative analysis of IL-4 level. (**E**) Quantitative analysis of IL-10 level. (**F**, **G**) Representative immunofluorescence staining of 8-OHG (red)/NeuN (green)/DAPI (blue) showing oxidative damage to neuronal DNA/RNA, and the quantitative analysis of mean fluorescence intensity of 8-OHG at perihematomal region at day 3. Scale bars: 50 μm. The data were exhibited as mean ± SEM, and analyzed by a one-way ANOVA with Tukey's multiple comparisons
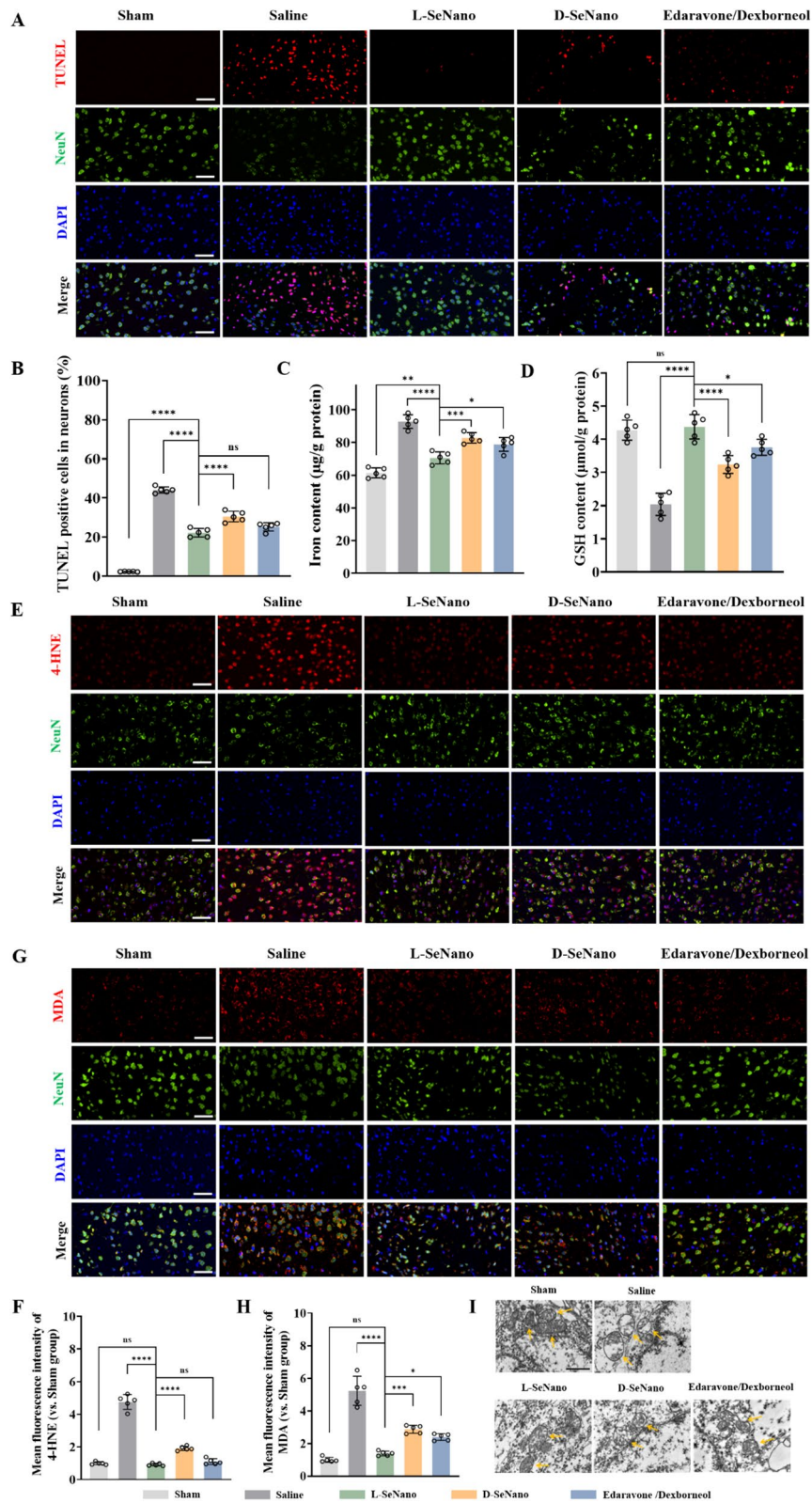
Fig. 6 (See legend on next page.)

(See figure on previous page.)

Fig. 6 Intervention effect of SeNano on neuronal apoptosis and ferroptosis following ICH. (**A**, **B**) Representative immunofluorescence staining of TUNEL (red)/NeuN (green)/DAPI (blue) at perihematomal region at day 3 reflecting neuronal apoptosis, and quantitative analysis of TUNEL positive cells in neurons. Scale bars: 50 µm. (**C**) Iron content tested by an iron assay kit at perihematomal region at day 3. (**D**) GSH content measured by a GSH assay kit at perihematomal region at day 3. (**E**, **F**) Representative immunofluorescence staining of 4-HNE (red)/NeuN (green)/DAPI (blue) at perihematomal region at day 3 reflecting lipid peroxide degree, and quantitative analysis of mean fluorescence intensity of 4-HNE. Scale bars: 50 µm. (**G**, **H**) Representative immunofluorescence staining of MDA (red)/NeuN (green)/DAPI (blue) at perihematomal region at day 3 reflecting lipid peroxide degree, and quantitative analysis of mean fluorescence intensity of MDA. Scale bars: 50 µm. The data were exhibited as mean ± SEM, and analyzed by a one-way ANOVA with Tukey's multiple comparisons

levels, and also alleviating oxidative damage to neuron, whose therapeutic effect was greater than D-SeNano group and Edaravone/Dexborneol group (clinically approved anti-oxidative/anti-inflammatory agent).

Next, we further investigated the effect of SeNano on programmed cell death of neuron. NeuN/TUNEL staining was performed at day 3 following ICH, showing that neuronal apoptosis was largely increased and it could be effectively inhibited by L-SeNano to restore neuronal signaling (Fig. 6A-B). Besides, excessive oxidative stress might trigger neuronal ferroptosis. Therefore, we continued to examine the typical ferroptosis features, where elevated iron content, downregulated GPX4 and GSH levels, were detected (Figs. 2F-G and 6C-D), implying that cellular antioxidant defense was impaired [36]. This contributed to the lipid peroxide accumulation in neurons as the relevant biomarkers 4-HNE and MDA were dramatically upregulated and distributed in neurons (Fig. 6E-H). Additionally, mitochondrial morphology changes, a key indicator of ferroptosis, were also observed by TEM, showing that mitochondrial morphology changed after ICH, such as mitochondrial membrane rupture and cristae reduction (Fig. 6I). This illustrated that neuronal ferroptosis was indeed induced. Upon treatment, it was demonstrated that the L-SeNano had a strong capability of normalizing these abnormal changes and inhibiting neuronal ferroptosis. Its performance in inhibiting programmed cell death of neurons, including apoptosis and ferroptosis, was superior to D-SeNano and Edaravone/Dexborneol treatments.

Underlying molecular mechanisms of multiple neuroprotective roles at acute phase

To reveal underlying molecular mechanisms of SeNano on neuroprotection at acute phase, brain tissues at perihematomal region were collected at day 3 upon various treatments to support bulk RNA sequencing. The unguided heatmaps of transcriptomic data showed markedly different mRNA profiles between SeNano and saline groups (Fig. S6A), where the genes with a $\log_2$ (fold change) ≥ 1.0 were considered to be statistically upregulated and ≤ −1.0 were downregulated (SeNano vs. saline groups). In detail, it was detected that L-SeNano treatment group exhibited 64 upregulated genes and 29 downregulated genes in comparison with saline group (Fig. 7A), while the D-SeNano group

exhibited 37 upregulated genes and 27 downregulated genes (Fig. S6B). Given that the findings about multiple neuroprotective roles of L-SeNano, we employed bioinformatics techniques to provide an in-depth understanding from the viewpoint of regulatory genes. Enrichment analysis indicated that the differentially expressed genes (DEGs) were associated with multiple Gene Ontology (GO) terms, which were grouped into biological process (BP), cellular component (CC), molecular function (MF), mainly including the oxoacid metabolic process, regulation of reactive oxygen species biosynthetic process, NF-kappa B signaling, regulation of apoptotic process, lipid metabolic process, microglial cell activation, astrocyte differentiation, and learning or memory (Fig. 7B). Further, Kyoto Encyclopedia of Genes and Genomes (KEGG) enrichment analysis suggested that L-SeNano regulated genes were enriched in various signaling pathways, such as inflammation-related pathways (TNF signaling pathway, IL-17 signaling pathway, NF-kappa B signaling), oxidative stress-related pathways (arachidonic metabolism, linoleic acid metabolism, glycerolipid metabolism, glyoxylate and dicarboxylate metabolism), microglia polarization-related pathways (arginine and proline metabolism), apoptosis-related pathways (TGF-β signaling pathway, Apelin pathway), and ferroptosis-related pathways (Hippo and Wnt signaling pathway [37, 38]) (Fig. 7C). Moreover, representative genes from relevant pathways were also detected in heatmap (Fig. 7D), where the upregulated genes included Dcn (TGF-β signaling pathway), Cdh1 (Apelin pathway) and downregulated genes included Glyctk (oxidative stress-related pathways), Rspo1 (Wnt signaling pathway), Ccl21b (inflammation-related pathways) [39]. By comparison, we observed that D-SeNano possessed similar regulatory pathways in terms of its moderate neuroprotective functions (Fig. S6C-E).

The RNA sequencing results preliminary revealed the molecular mechanism that underlay multiple neuroprotective effects of L-SeNano at acute phase, including inhibiting glial cells overactivation, producing the anti-inflammatory niche of microglia, suppressing inflammatory response and oxidative damage, then alleviating neuronal apoptosis and ferroptosis. This was in line with the immunofluorescence staining results observed in vivo.
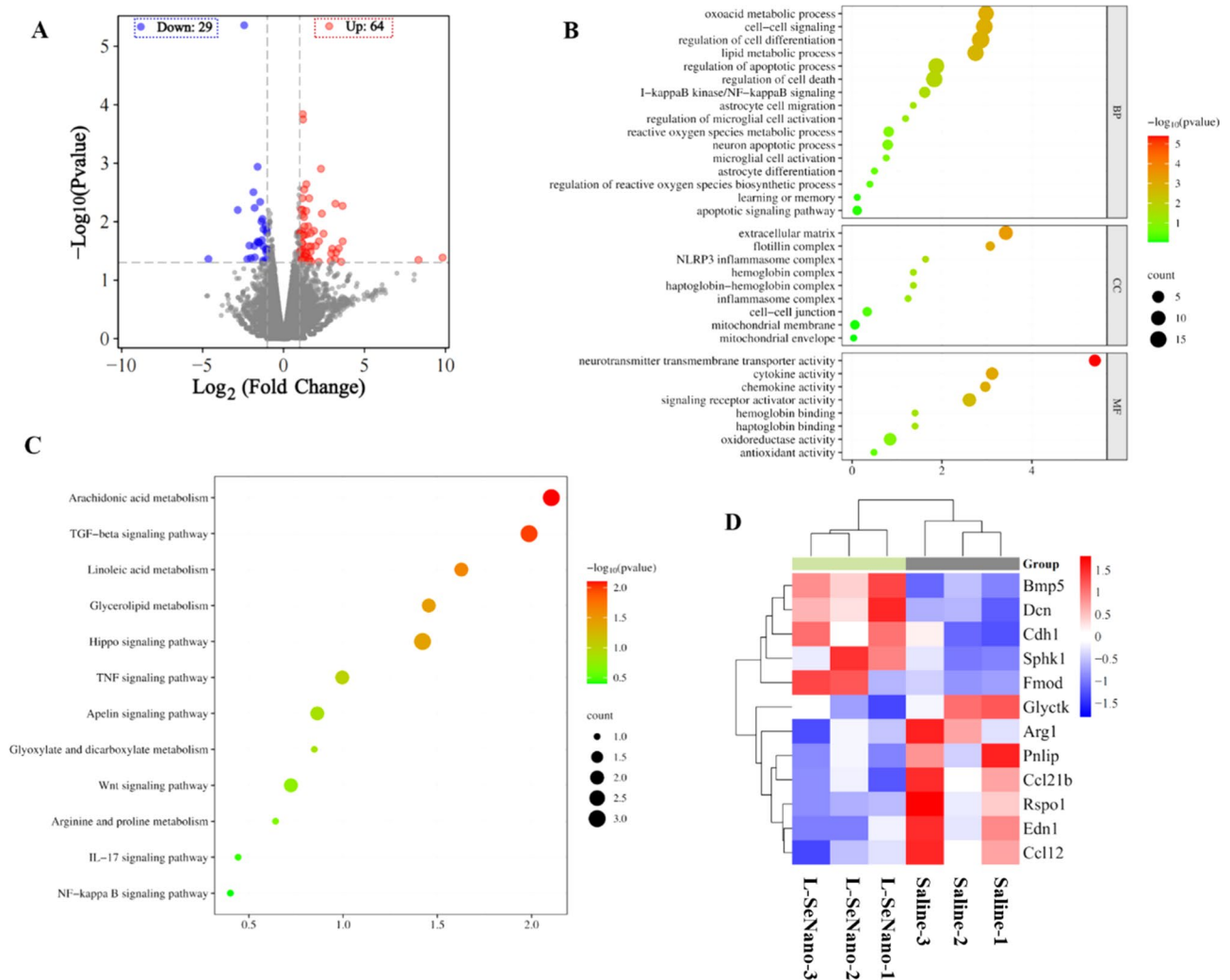
Fig. 7 Bulk RNA sequencing analysis to reveal neuroprotection mechanism of L-SeNano at acute phase. (**A**) Volcano plots for all differentially expressed genes (DEGs) between L-SeNano and saline group (*n* = 3 independent samples). Dots represented DEGs (*P* < 0.05, at least 2-fold difference). Red and blue indicated upregulation and downregulation, respectively. (**B**) Enrichment analysis of GO term between L-SeNano and saline group. (**C**) Enrichment analysis of KEGG pathway between L-SeNano and saline group. (**D**) Heatmap of representative genes of relevant pathways

Intervention effect of SeNano on neurogenesis and glial scar at recovery phase

At recovery phase, the key pathological processes, mainly including the adult neurogenesis dysfunction and glial scar formation, heavily impeded the repair of injuried brain. At day 28 following ICH, immunofluorescence staining results exhibited that number of newly divided neural precursor cells (DCX/BrdU double positive cells) at subventricular zone (SVZ), and number of newly divided neurons at perihematomal region (NeuN/BrdU double positive cells) were extremely low (Fig. 8A-D), which illustrated that neurogenesis event was weak and against brain repair. In addition, considering that the astrocyte constantly proliferated during recovery phase and formed a long-term structural alteration of glial scar, we found that the numerous astrocytes accumulated at perihematomal region and obviously formed the glial scar (Fig. 8E-F), which would hamper the remodeling of injuried brain and lead to an irreversible SBI.

L-SeNano treatment enabled pathological process at recovery phase to be obviously altered. It was observed that proliferating neural precursor cells at SVZ and neurons at perihematomal region were significantly increased, oxidative state of neural precursor cells was relieved due to the downregulation of NADPH oxidase 2 (NOX2) and oxidative damage marker 8-OHG (Fig. S7 and S8), and meanwhile the glial scar was inhibited and even achieved a similar level as sham group. This demonstrated that L-SeNano largely promoted neurogenesis and inhibited glial scar, which were beneficial for the repair of injured brain and neurofunctional reconstruction.
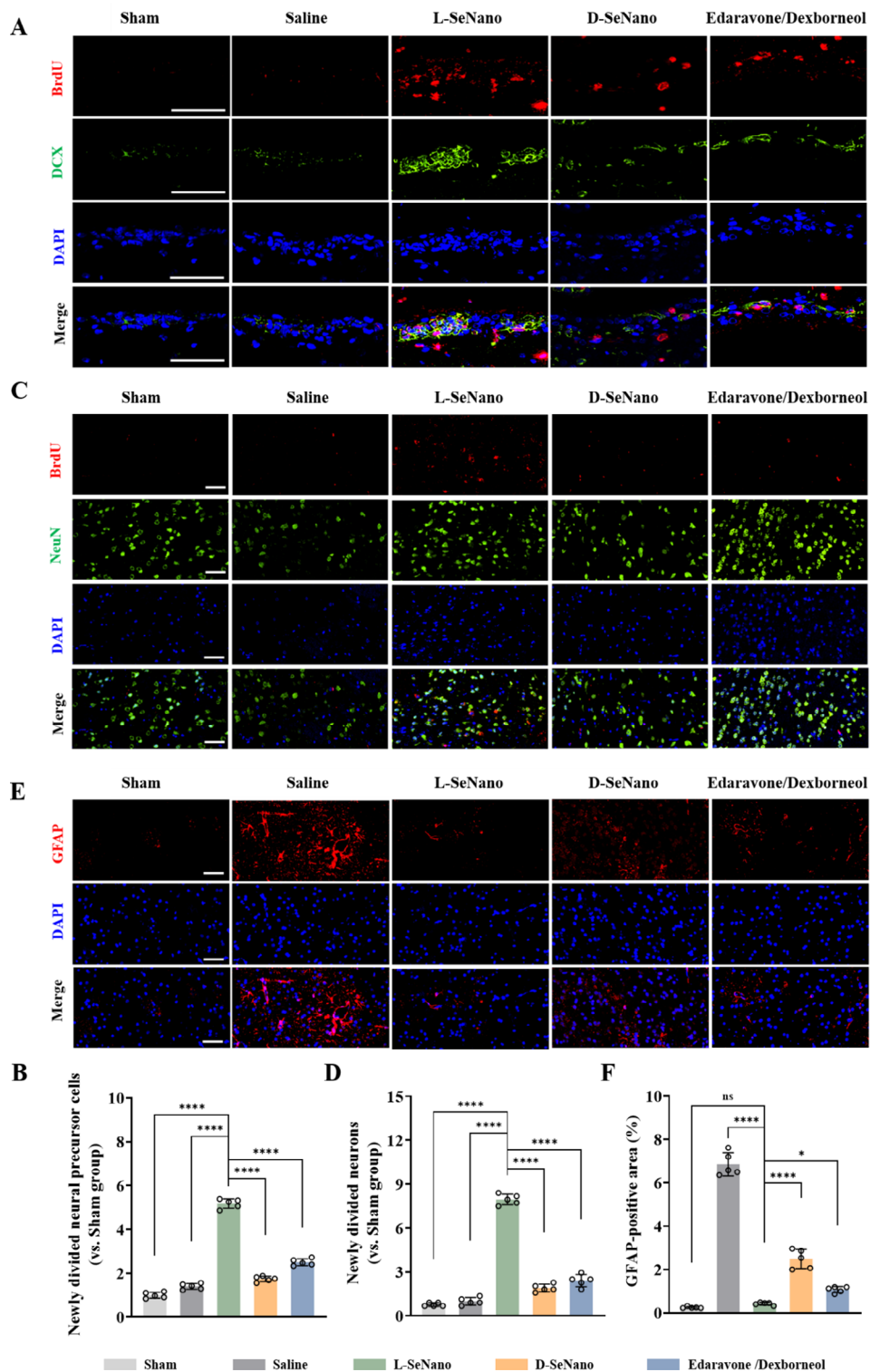
Fig. 8 Intervention effect of SeNano on neurogenesis and glial scar following ICH. (**A**, **B**) Representative immunofluorescence staining of BrdU (red)/DCX (green)/DAPI (blue) at SVZ at day 28 reflecting proliferating neural precursor cells, and quantitative analysis of newly divided neural precursor cells. Scale bars: 50 μm. (**C**, **D**) Representative immunofluorescence staining of BrdU (red)/NeuN (green)/DAPI (blue) at perihematomal region at day 28 reflecting proliferating neurons, and quantitative analysis of newly divided neurons. Scale bars: 50 μm. (**E**, **F**) Representative immunofluorescence staining of GFAP (red)/DAPI (blue) at perihematomal region at day 28 reflecting glial scar formation, and quantitative analysis of GFAP positive area. Scale bars: 50 μm. The data were exhibited as mean ± SEM, and analyzed by a one-way ANOVA with Tukey's multiple comparisons

Underlying molecular mechanism of enhancing neurogenesis and inhibiting glial scar at recovery phase

To elucidate underlying molecular mechanisms of SeNano on enhancing neurogenesis and inhibiting glial scar formation at recovery phase, the brain tissues at perihematomal region and SVZ were collected again 28 days post of ICH for bulk RNA sequencing analysis. Upon SeNano treatment, mRNA profiles of brain tissues were significantly changed from the unguided heatmaps results (Fig. S9A). Among them, L-SeNano treatment group contained 94 DEGs with 61 upregulated and 33 downregulated genes (Fig. 9A), while D-SeNano

treatment resulted in 137 DEGs with 124 upregulated and 13 downregulated genes (Fig. S9B). Further, the bioinformatics techniques were performed to reveal the molecular mechanisms of SeNano in modulating neurogenesis and glial scar. GO term analysis showed that L-SeNano treatment involved neural precursor cell proliferation, regulation of stem cell proliferation, cell activation, and learning or memory (Fig. 9B). Nevertheless, biological functions of D-SeNano primarily focused on cell activation, cell killing, astrocyte differentiation (Fig. S9C). Besides, enrichment analysis of KEGG indicated that the L-SeNano modulated multiple pathways closely related
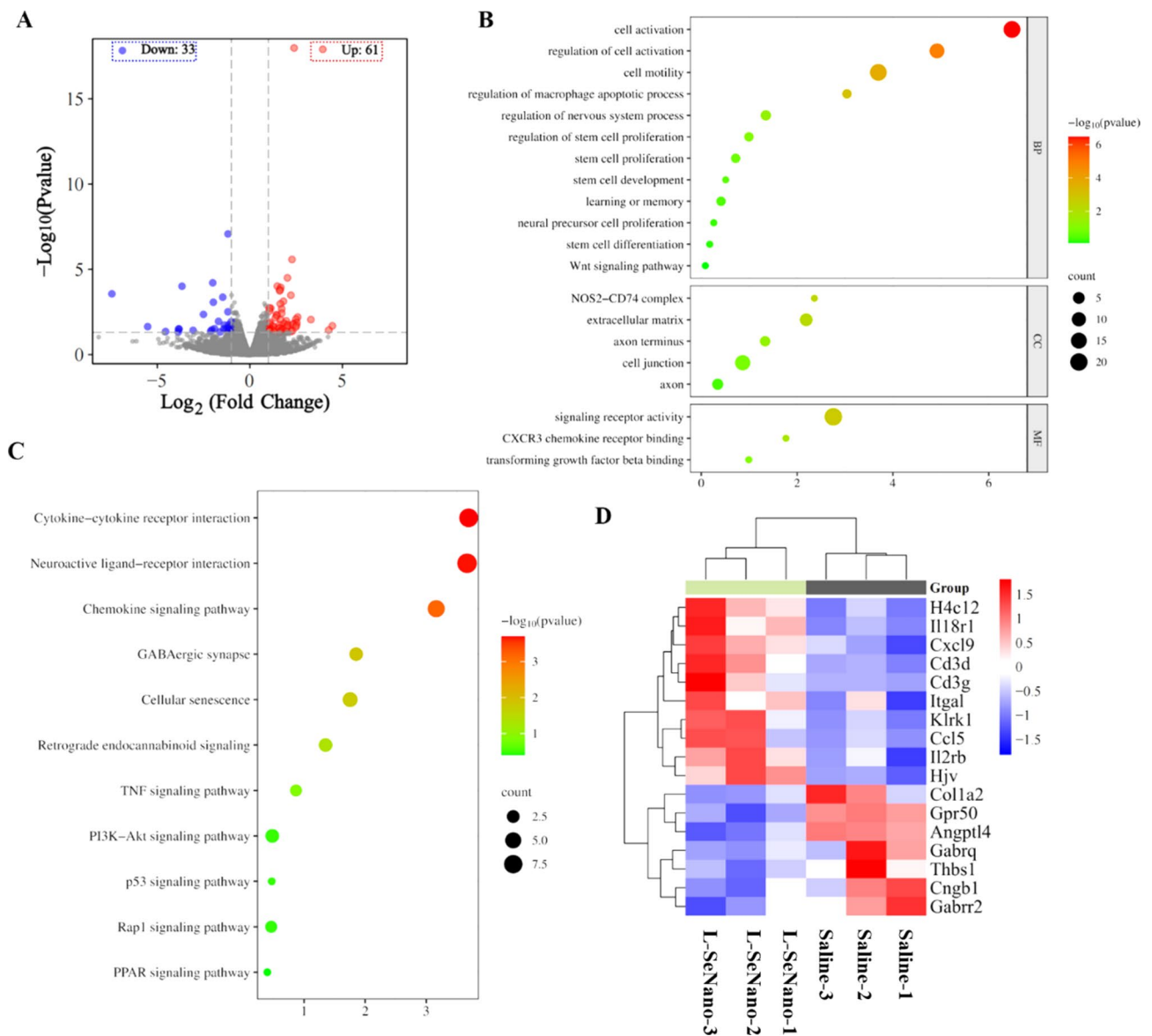

Fig. 9 Bulk RNA sequencing analysis to elucidate molecular mechanism of L–SeNano about promoting neurogenesis and inhibiting glial scar at recovery phase. (**A**) Volcano plots for all differentially expressed genes (DEGs) between L-SeNano and saline group (*n* = 3 independent samples). Dots represented DEGs (*P* < 0.05, at least 2-fold difference). The red and blue indicated upregulation and downregulation, respectively. (**B**) Enrichment analysis of GO term between L-SeNano and saline group. (**C**) Enrichment analysis of KEGG pathway between L-SeNano and saline group. (**D**) Heatmap of representative genes of relevant pathways

to neurogenesis and glial scar, such as cytokine-cytokine receptor interaction, neuroactive ligand-receptor interaction, GABAergic synapse, PI3K-Akt signaling pathway (Fig. 9C). Then, the heatmap of representative genes participating in relevant pathways was depicted in Fig. 9D. Neural precursor cells synthesized and released GABA to regulate migration and proliferation of neuroblasts, acting as a negative regulator of neurogenesis [40]. And, the downregulation of genes involved in the GABAergic synapse, such as Gpr50, Gabrr2, Gabrq, might have implications for neurogenesis. Also, the downregulated genes, Colla2 and Thbs1, could inhibit the activation of PI3K/Akt pathway to prevent glial scar formation. Additionally, Itgal and H4c12 were upregulated to enhance the neuroactive ligand-receptor interactions that were associated with neurogenesis and learning memory function [41, 42]. For D-SeNano treatment, KEGG analysis showed that the regulatory pathways were mainly focused on cellular senescence as well as chemokine signaling pathway, with the fewer pathways and representative genes involved in promoting neural regeneration and inhibiting glial scar formation (Fig. S9D-E). These results preliminary elucidated the molecular mechanism of L- SeNano that promoted neurogenesis and inhibited glial scar at recovery phase.

Combinational therapeutic effect of SeNano on SBI and neurobehavioral functions

All above results confirmed that L-SeNano could effectively exert multiple neuroprotective roles at acute phase, and enhance neurogenesis as well as inhibit glial scar formation at recovery phase, providing an evident prediction for the combinational therapy. Next, therapy effect was evaluated by the changes of neuroanatomical structures and neurobehavioral functions upon treaments. Nissl staining was firstly performed to observe nissl bodies in the cytoplasm of neurons, which was an indicator of neuronal integrity and number. In comparison with sham group, the saline-treated ICH mice was observed with a remarkable decrease of nissl positive neurons at perihematomal region at day 3, and maintained a low positive cell number (<30) until day 28, which confirmed that ICH resulted in a severe secondary damage to functional neurons (Fig. 10A-B). Fortunately, upon L-SeNano treatment, the nissl positive neurons were increased to ~60 at day 3 due to multiple neuroprotective roles, and sustainably increased to ~82 at day 14 and ~106 at day 28 owing to the driven neurogenesis process, which contributed to the recovery to a normal level (Fig. 10A-B), implying excellent therapy effect on the integrity and number of neurons at perihematomal region, and thereby well preventing SBI. Nevertheless, it was also found that D-SeNano and Edaravone/Dexborneol treatments exhibited the fewer nissl positive neurons until day 28 due

to their weaker modulations on neuroprotection and neurogenesis.

Furthermore, for the purpose of exploring therapy effect on neurobehavioral functions, we performed neurological score and behavior tests to investigate short and long-term recovery of neurological deficits following ICH (Fig. 10C). Herein, modified neurologic severity score (mNSS) was used to assess sensorimotor dysfunction. We observed that saline- treated mice exhibited a high mNSS score, demonstrating a severe damage to the sensorimotor function. Upon L-SeNano treatment, mNSS score was gradually decreased and close to a normal level at day 14, well reversing neurological deficit of ICH mice (Fig. 10D). Besides, to further evaluate motor behavior and physical activity level, open field test was also performed where the total distance traveled and velocity were carefully traced to reflect the locomotion. It was obviously monitored that L-SeNano treatment remarkably increased the total travelled distance and mean speed in comparison with saline group, and even increased to a normal level at day 28, indicating that their physical activity level could be recovered by L-SeNano treatment within one month (Fig. 10E-G).

Spatial working memory dysfunction was also a common sequela of ICH, and thus it was tested through spontaneous alternation task in Y maze (Fig. 10H), showing that the L-SeNano treatment enabled alternation rate to be persistently increased, and there were no significant differences in alternation rate compared with sham group at day 28 (Fig. 10I and S10), implying that their spatial working memory was fully recovered.

Taken together, we found that the ICH mice treated with L-SeNano achieved better neurofunctional performances in above mNSS, open field and Y maze experiments than D-SeNano and Edaravone/Dexborneol groups, which recovered neuroanatomical structures and neurobehavioral functions. This could demonstrate the superiority of combinational therapy based on the dual-modulating neuroprotection and neurogenesis, over traditional monotherapy based on neuroprotection.

Biosafety assessment

Biosafety was also an important evaluation criterion for clinical applications, and thus we systematically assessed the biosafety of SeNano at cell, organ and blood levels, respectively. Firstly, the cytotoxicity of SeNano was evaluated by a standard Cell Counting Kit-8 (CCK-8) assay. Different concentrations of SeNano were incubated with various types of relevant cells, including mouse brain microvascular endothelial cells (Bend.3), mouse microglial cells (BV2) and mouse hippocampal neuronal cells (HT22). After 24 h of incubation, all these cells achieved>80% viability when the SeNano were even at high concentration of 200 μg/mL (Fig. 11A-B), indicating
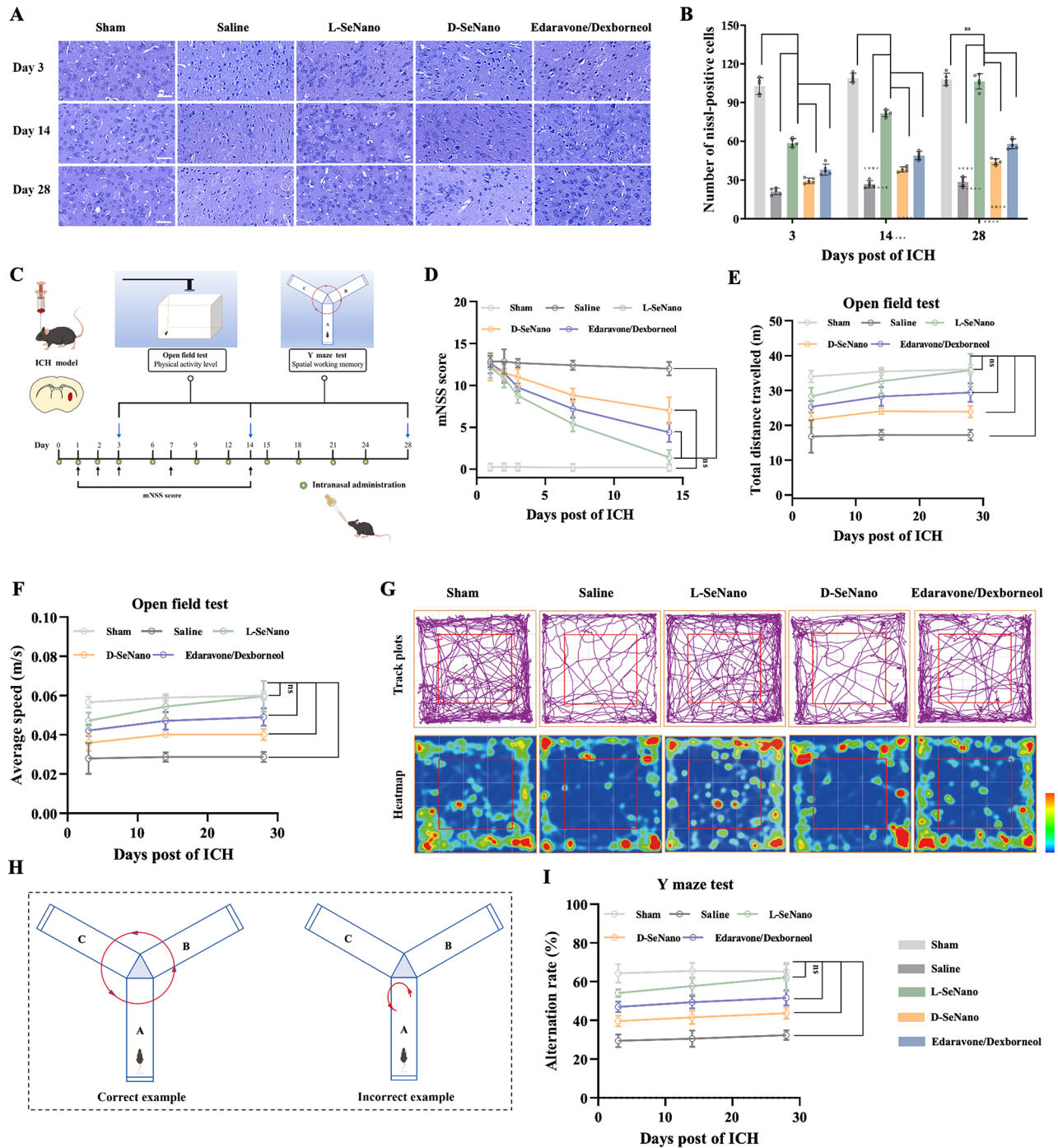
Fig. 10 Combinational therapeutic effect of SeNano on neurofunctional recovery following ICH. (**A**, **B**) Representative Nissl staining at perihematomal region at different time points showing changes of neuronal structure and number, and quantitative analysis of the number of nissl positive cells. Scale bars: 50 μm. (**C**) Schematic illustration of the mNSS score, open filed test, and Y maze test. (**D**) Quantitative assessment of sensorimotor dysfunction using mNSS score at different time points. (**E**) Total distance travelled during 10 min of open field test at different time points. (**F**) Average speed during 10 min of open field test at different time points. (**G**) Representative track plot and heatmap of the open field test at day 28 following ICH. (**H**) Example of spontaneous alternations in Y maze test (correct vs. incorrect). (**I**) Spontaneous alteration rate in Y maze test at different time points. The data were exhibited as mean ± SEM, and analyzed by a one-way ANOVA with Tukey's multiple comparisons
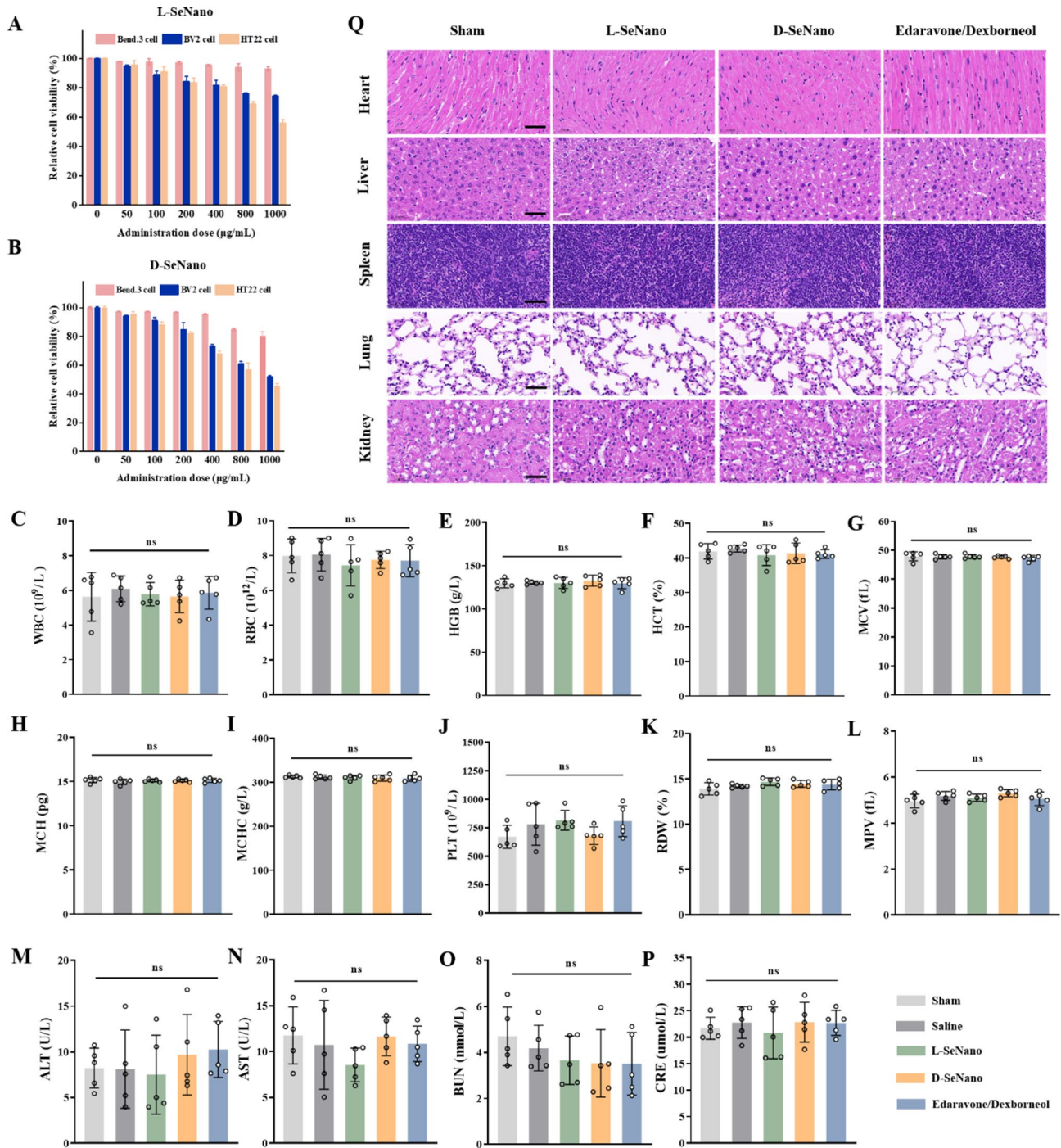
Fig. 11 Biosafety assessment of SeNano at cell, blood and organ levels following ICH. (**A**, **B**) Cytotoxicity of L-SeNano and D-SeNano to Bend.3, BV2 and HT22 cells evaluated by CCK-8 assays. (**C-P**) Side effects on blood cells and liver, kidney functions examined by the blood routine and biochemical tests, incluidng (**C**) WBC, (**D**) RBC, (**E**) HGB, (**F**) HCT, (**G**) MCV, (**H**) MCH, (**I**) MCHC, (**J**) PLT, (**K**) RDW, (**L**) MPV, (**M**) ALT, (**N**) AST, (**O**) BUN, (**P**) CRE. (**Q**) Representative H&E staining of primary organs, including heart, liver, spleen, lung, kidney, reflecting their injury situation. Scale bars: 50 μm. The data were exhibited as mean ± SEM, and analyzed by a one-way ANOVA with Tukey's multiple comparisons

that there was almost no obvious toxicity to brain microvascular endothelial cells, microglial cells and neurons. Secondly, upon 28 days of drug administration, blood routine and biochemical tests were performed using the blood from tail vein, and results showed that there were no significant differences for routine hematology markers and alanine aminotransferase (ALT), aspartate transaminase (AST), blood urea nitrogen (BUN), and creatinine levels between SeNano groups and sham group (Fig. 11C-P), indicating SeNano administration had an

ignorable influence on the blood cells and liver, kidney functions. To further study the potential side effect on organ injury, mice was sacrificed to harvest the primary organs (including heart, liver, spleen, lung and kidney) for H&E staining. Results revealed that SeNano treatment didn't induce obvious damages or morphological changes to these organs (Fig. 11Q), accompanied with the therapeutic administration dose, which was equative to the sham group and clinically approved drug Edaravone/ Dexborneol group. By the above safety examinations, we confirmed that SeNano were biologically safe, which was beneficial for the subsequent clinical applications.

Conclusions

To achieve the primary therapeutic goal of minimizing SBI and restoring neurobehavioral functions following hemorrhagic stroke, this work proposed a new combinational therapeutic strategy of neuroprotection and neurogenesis. To this end, we rationally designed L-SeNano and found that it had the multi-therapeutic-activity to modulate neuroprotection and enhance neurogenesis. In summary, L-SeNano exhibited superiorities of facile preparation, high stability and low cost. More importantly, intranasal administration of L-SeNano could not only exert multiple neuroprotective roles at acute phase by inhibiting the glial cells overactivation, producing anti-inflammatory niche, suppressing inflammatory response and oxidative damage, then alleviating neuronal apoptosis/ ferroptosis, but further promote neuronal repair at recovery phase by driving neurogenesis and inhibiting glial scar formation, which prevented SBI and recovered neurobehavioral functions, and even reached a similar level as healthy mice. The combinational therapeutic effect was significantly better than the clinically applicable neuroprotective agent Edaravone/Dexborneol. In addition, it also acquired satisfactory safety. This study offered a new avenue to develop the next-generation pharmacotherapy for effective hemorrhagic stroke management.

Abbreviations

SBI	Secondary Brain Injury
SeNano	Selenium Nanodot
ICH	Intracerebral Hemorrhage
BBB	Blood-Brain Barrier
DCFH-DA	Dichlorodihydrofluorescein Diacetate
DAPI	4', 6-Diamidino-2-Phenylindole Dihydrochloride
DMEM	Dulbecco's Modified Eagle Medium (DMEM)
FBS	Fetal Bovine Serum (FBS)
CCK-8	Cell Counting Kit-8
XPS	X-Ray Photoelectron Spectroscopy
ICP-MS	Inductively Coupled Plasma -Mass Spectrometry
mNSS	Modified Neurologic Severity Score
TEM	Transmission Electron Microscopy
ROS	Reactive Oxygen Species
MFI	Mean Fluorescence Intensity
DEGs	Differentially Expressed Genes
BP	Biological Process
CC	Cellular Component
MF	Molecular Function
GO	Gene Ontology
KEGG	Kyoto Encyclopedia of Genes and Genomes

Author contributions

Bin Gao, Dezhi Kang, Yuanxiang Lin proposed and supervised the project. Bin Gao, Yibin Zhang prepared ASPM. Bin Gao, Yibin Zhang, Xuegang Niu, Chunwang Li, and Huimin Wang performed the physicochemical characterizations. Yibin Zhang, Xiaoyu Wang, Haojie Wang, Yi Wu performed in vitro and in vivo intervention effects and biosafety. Yibin Zhang performed intervention mechanism experiments. Bin Gao, Yibin Zhang, Xiaoyu Wang, Shen Lin, Dengliang Wang, Fuxin Lin, Peisen Yao contributed to disscusions about experimental results. Bin Gao, Yibin Zhang wrote this manuscript and supplementary materials. All authors have given approval to the final version of the manuscript.

Declarations

Ethics approval and consent to participate

The animal experiments were conducted according to Animal Protection Guidelines of Fujian Medical University (IACUC FJMU 2024-Y-0857), which were also conformed to the "Guide for the Protection and Use of Experimental Animals" of American National Institutes of Health.

Consent for publication

Not applicable.

Competing interests

The authors declare no competing interests.

Author details

[1]Department of Neurosurgery, Neurosurgery Research Institute, The First Affiliated Hospital, Fujian Medical University, Fuzhou, Fujian 350005, China [2]Fujian Provincial Institutes of Brain Disorders and Brain Sciences, The First Affiliated Hospital, Fujian Medical University, Fuzhou, Fujian 350005, China [3]Fujian Provincial Clinical Research Center for Neurological Diseases, The First Affiliated Hospital, Fujian Medical University, Fuzhou, Fujian 350005, China [4]Department of Neurosurgery, National Regional Medical Center, Binhai Campus of the First Affiliated Hospital, Fujian Medical University, Fuzhou 350212, China [5]College of Materials Science and Engineering, Qingdao University, Qingdao 266071, China

Zhang *et al. Journal of Nanobiotechnology*   (2024) 22:564

Page 22 of 23

References

1. Collaborators GBDS. Global, regional, and national burden of stroke and its risk factors, 1990–2019: a systematic analysis for the global burden of Disease Study 2019. Lancet Neurol. 2021;20:795–820.
2. Puy L, Parry-Jones AR, Sandset EC, Dowlatshahi D, Ziai W, Cordonnier C. Intracerebral haemorrhage. Nat Rev Dis Primers. 2023;9:14.
3. Morotti A, Boulouis G, Dowlatshahi D, Li Q, Shamy M, Al-Shahi Salman R, Rosand J, Cordonnier C, Goldstein JN, Charidimou A. Intracerebral haemorrhage expansion: definitions, predictors, and prevention. Lancet Neurol. 2023;22:159–71.
4. Sheth KN, Selim M. Focused update on vascular risk and secondary prevention in survivors of intracerebral hemorrhage. Stroke. 2022;53:2128–30.
5. Li Z, Li Y, Han i, Zhu Z, Li M, Liu Q, Wang Y, Shi F-D. Formyl peptide receptor 1 signaling potentiates inflammatory brain injury. Sci Transl Med. 2021;13:eabe9890.
6. Xue M, Yong VW. Neuroinflammation in intracerebral haemorrhage: immunotherapies with potential for translation. Lancet Neurol. 2020;19:1023–32.
7. Kuramatsu JB, Biffi A, Gerner ST, Sembill JA, Sprugel MI, Leasure A, Sansing L, Matouk C, Falcone GJ, Endres M, et al. Association of surgical hematoma evacuation vs conservative treatment with functional outcome in patients with cerebellar intracerebral hemorrhage. JAMA. 2019;322:1392–403.
8. Yang M, Deng S, Jiang J, Tian M, Xiao L, Gong Y. Oxytocin improves intracerebral hemorrhage outcomes by suppressing neuronal pyroptosis and mitochondrial fission. Stroke. 2023;54:1888–900.
9. Lin SH, Huang APH. Hsu Sh. Injectable, micellar chitosan self-healing hydrogel for asynchronous dual-drug delivery to treat stroke rats. Adv Funct Mater. 2023;33:2303853.
10. Han R, Lan X, Han Z, Ren H, Aafreen S, Wang W, Hou Z, Zhu T, Qian A, Han XN, Koehler RC, Liu GS. Improving outcomes in intracerebral hemorrhage through microglia/macrophage-targeted IL-10 delivery with phosphatidyl-serine liposomes. Biomaterials. 2023;301:122277.
11. Dharmalingam P, Talakatta G, Mitra J, Wang H, Derry PJ, Nilewski LG, McHugh EA, Fabian RH, Mendoza K, Vasquez V, Hegde PM, Kakadiaris E, Roy T, Boldogh I, Hegde VL, Mitra S, Tour JM, Kent TA, Hegde ML. Pervasive genomic damage in experimental intracerebral hemorrhage: therapeutic potential of a mechanistic-based carbon nanoparticle. ACS Nano. 2020;14:2827–46.
12. Yuan T, Wang T, Zhang J, Shi S, Gu Z, Li Y, Xu J. Procyanidins boost the neuroprotective effect of minocycline for intracerebral haemorrhage. Adv Funct Mater. 2023;33:2303379.
13. Huang G, Zang J, He L, Zhu H, Huang J, Yuan Z, Chen T, Xu A. Bioactive nanoenzyme reverses oxidative damage and endoplasmic reticulum stress in neurons under ischemic stroke. ACS Nano. 2022;16:431–52.
14. Zhang X, Huang X, Hang D, Jin J, Li S, Zhu Y, Liu H. Targeting pyroptosis with nanoparticles to alleviate neuroinflammatory for preventing secondary damage following traumatic brain injury. Sci Adv. 2024;10:eadj4260.
15. Yang H, Han M, Li J, Ke H, Kong Y, Wang W, Wang L, Ma W, Qiu J, Wang X, Xin T, Liu H. Delivery of miRNAs through metal-organic framework nanoparticles for assisting neural stem cell therapy for ischemic stroke. ACS Nano. 2022;16:14503–16.
16. Yoo AS, Staahl BT, Chen L, Crabtree GR. MicroRNA-mediated switching of chromatin-remodelling complexes in neural development. Nature. 2009;460:642–6.
17. Liddle LJ, Ralhan S, Ward DL, Colbourne F. Translational intracerebral hemorrhage research: has current neuroprotection research ARRIVEd at a standard for experimental design and reporting? Transl Stroke Res. 2020;11:1203–13.
18. Toyoda K, Yoshimura S, Nakai M, Koga M, Sasahara Y, Sonoda K, Kamiyama K, Yazawa Y, Kawada S, Sasaki M, Terasaki T, Miwa K, Koge J, Ishigami A, Wada S, Iwanaga Y, Miyamoto Y, Minematsu K, Kobayashi S. Twenty-year change in severity and outcome of ischemic and hemorrhagic strokes. JAMA Neurol. 2022;79:61–9.
19. Yu W, Liu B, Zhou L, Gong E, Che C, Zhou J, Zhang Z, Liu J, Shi J. The development of drug delivery systems for efficient intracranial hemorrhage therapy. Adv Healthc Mater. 2023;12:e2203141.
20. Modo MM, Jolkkonen J, Zille M, Boltze J. Future of animal modeling for post-stroke tissue repair. Stroke. 2018;49:1099–106.
21. Eltzschig HK, Eckle T. Ischemia and reperfusion–from mechanism to translation. Nat Med. 2011;17:1391–401.
22. Zou B, Xiong Z, Yu Y, Shi S, Li X, Chen T. Rapid selenoprotein activation by selenium nanoparticles to suppresses osteoclastogenesis and pathological bone loss. Adv Mater. 2024;36:e2401620.
23. Alim I, Caulfield JT, Chen Y, Swarup V, Geschwind DH, Ivanova E, Seravalli J, Ai Y, Sansing LH, Ste Marie EJ, Hondal RJ, Mukherjee S, Cave JW, Sagdullaev BT, Karuppagounder SS, Ratan RR. Selenium drives a transcriptional adaptive program to block ferroptosis and treat stroke. Cell. 2019;177:1262–79.
24. Xu R, You Y, Zheng W, Ma L, Chang Y, Pan S, He Y, Zhou M, Xu Z, Chen T, Liu H. Selenoprotein-regulated hydrogel for ultrasound-controlled microenvironment remodeling to promote bone defect repair. Adv Funct Mater. 2024;34:2313122.
25. Leiter O, Zhuo Z, Rust R, Wasielewska JM, Gronnert L, Kowal S, Overall RW, Adusumilli VS, Blackmore DG, Southon A, Ganio K, Mcdevitt CA, Rund N, Brici D, Mudiyan IA, Sykes AM, Rünker AE, Zocher S, Ayton S, Bush AI, Bartlett PF, Hou ST, Kempermann G, Walker TL. Selenium mediates exercise-induced adult neurogenesis and reverses learning deficits induced by hippocampal injury and aging. Cell Metab. 2022;34:408–23.
26. Ouyang J, Deng B, Zou B, Li Y, Bu Q, Tian Y, Chen M, Chen W, Kong N, Chen T, Tao W. Oral hydrogel microbeads-mediated in situ synthesis of selenoproteins for regulating intestinal immunity and microbiota. J Am Chem Soc. 2023;145:12193–205.
27. Reyes-Esteves S, Nong J, Glassman PM, Omo-Lamai S, Ohashi S, Myerson JW, Zamora ME, Ma X, Kasner SE, Sansing L, Muzykantov VR, Marcos-Contreras OA, Brenner JS. Targeted drug delivery to the brain endothelium dominates over passive delivery via vascular leak in experimental intracerebral hemorrhage. J Control Release. 2023;356:185–95.
28. Liebner S, Dijkhuizen RM, Reiss Y, Plate KH, Agalliu D, Constantin G. Functional morphology of the blood-brain barrier in health and disease. Acta Neuropathol. 2018;135:311–36.
29. Li F, Li TY, Sun CX, Xia JH, Jiao Y, Xu HP. Selenium-doped carbon quantum dots for free-radical scavenging. Angew Chem Int Ed. 2017;56:9910–4.
30. Shi SX, Shi K, Liu Q. Brain injury instructs bone marrow cellular lineage destination to reduce neuroinflammation. Sci Transl Med. 2021;13:eabc7029.
31. Xu M, Qi Y, Liu G, Song Y, Jiang X, Du B. Size-dependent *in vivo* transport of nanoparticles: implications for delivery, targeting, and clearance. ACS Nano. 2023;17:20825–49.
32. Li F, Li Y, Yang X, Han X, Jiao Y, Wei T, Yang D, Xu H, Nie G. Highly fluorescent chiral N-S-doped carbon dots from cysteine: affecting cellular energy metabolism. Angew Chem Int Ed. 2018;57:2377–82.
33. Liu Y, Tan Y, Cheng G, Ni Y, Xie A, Zhu X, Yin C, Zhang Y, Chen T. Customized intranasal hydrogel delivering methylene blue ameliorates cognitive dysfunction against alzheimer's disease. Adv Mater. 2024;36:e2307081.
34. Rebelo C, Reis T, Guedes J, Saraiva C, Rodrigues AF, Simoes S, Bernardino L, Peca J, Pinho SLC, Ferreira L. Efficient spatially targeted gene editing using a near-infrared activatable protein-conjugated nanoparticle for brain applications. Nat Commun. 2022;13:4135.
35. Lee MR, Shnitko TA, Blue SW, Kaucher AV, Winchell AJ, Erikson DW, Grant KA, Leggio L. Labeled oxytocin administered via the intranasal route reaches the brain in rhesus macaques. Nat Commun. 2020;11:2783.
36. Li C, Wu Y, Chen Q, Luo Y, Liu P, Zhou Z, Zhao Z, Zhang T, Su B, Sun T, Jiang C. Pleiotropic microenvironment remodeling micelles for cerebral ischemia-reperfusion injury therapy by inhibiting neuronal ferroptosis and glial overactivation. ACS Nano. 2023;17:18164–77.
37. Fu M, Hu Y, Lan T, Guan KL, Luo T, Luo M. The Hippo signalling pathway and its implications in human health and diseases. Signal Transduct Target Ther. 2022;7:376.
38. Holzem M, Boutros M, Holstein TW. The origin and evolution of wnt signalling. Nat Rev Genet. 2024;25:500–12.
39. Zhang W, Liu Y, Wang Z, He S, Liu W, Wu Y, Yang L, Hu C, Wang Y. Remodeling brain pathological microenvironment to lessen cerebral ischemia injury by multifunctional injectable hydrogels. J Control Release. 2024;369:591–603.
40. Marques BL, Carvalho GA, Freitas EMM, Chiareli RA, Barbosa TG, Di Araujo AGP, Nogueira YL, Ribeiro RI, Parreira RC, Vieira MS, Resende RR, Gomez RS, Oliveira-Lima OC, Pinto MCX. The role of neurogenesis in neurorepair after ischemic stroke. Semin Cell Dev Biol. 2019;95:98–110.
41. Zhang X, Li H, Wang H, Zhang Q, Deng X, Zhang S, Wang L, Guo C, Zhao F, Yin Y, Zhou TY, Zhong J, Feng H, Chen W, Zhang J, Feng H, Hu R. Iron/ROS/Itga3 mediated accelerated depletion of hippocampal neural stem cell pool contributes to cognitive impairment after hemorrhagic stroke. Redox Biol. 2024;71:103086.

42. Nicaise AM, D'Angelo A, Ionescu RB, Krzak G, Willis CM, Pluchino S. The role of neural stem cells in regulating glial scar formation and repair. Cell Tissue Res. 2022;387:399–414.

Publisher's note

Springer Nature remains neutral with regard to jurisdictional claims in published maps and institutional affiliations.